Cellular and Molecular Life Sciences (2021) 78:5807–5826
https://doi.org/10.1007/s00018-021-03879-7

Cellular and Molecular Life Sciences

ORIGINAL ARTICLE

Vinculin-mediated axon growth requires interaction with actin but not talin in mouse neocortical neurons

Pranay Mandal[1] · Vivek Belapurkar[1] · Deepak Nair[1] · Narendrakumar Ramanan[1]

Received: 29 December 2020 / Revised: 12 May 2021 / Accepted: 11 June 2021 / Published online: 20 June 2021

Abstract

The actin-binding protein vinculin is a major constituent of focal adhesion, but its role in neuronal development is poorly understood. We found that vinculin deletion in mouse neocortical neurons attenuated axon growth both in vitro and in vivo. Using functional mutants, we found that expression of a constitutively active vinculin significantly enhanced axon growth while the head-neck domain had an inhibitory effect. Interestingly, we found that vinculin-talin interaction was dispensable for axon growth and neuronal migration. Strikingly, expression of the tail domain delayed migration, increased branching, and stunted axon. Inhibition of the Arp2/3 complex or abolishing the tail domain interaction with actin completely reversed the branching phenotype caused by tail domain expression without affecting axon length. Super-resolution microscopy showed increased mobility of actin in tail domain expressing neurons. Our results provide novel insights into the role of vinculin and its functional domains in regulating neuronal migration and axon growth.

Keywords Axon Growth · Neurite branching · Neuronal migration · Vinculin · Talin

Introduction

Neuronal migration, axon growth, and extension are intricately regulated processes that must be strictly coordinated for the normal structural and functional development of the mammalian brain. These require coordination of the cellular cytoskeleton at the leading processes during neuronal migration and at the growth cone during axon growth [1, 2]. The growth cone at the axon tip is a highly dynamic structure that constantly interacts with the environment. The growth cone movements are aided by the formation of actin-rich membranous structures called lamellipodia and filopodia [3]. These structures are driven by continuous polymerisation and depolymerisation of the actin cytoskeleton. The actin cytoskeletal dynamics are regulated by several actin-binding proteins [4], which mediate polymerisation, depolymerisation, and branching of actin filaments.

A critical first step in the growth and extension of neurites is filopodia formation. Filopodia are F-actin-rich structures that are essential for neurite formation and growth [5]. Studies have shown that neurons that lack critical actin-binding proteins showed attenuated neuritogenesis and axon growth [6]. Extension of the cell membrane and growth of axon requires the constant engagement of the actin cytoskeleton with the extracellular matrix (ECM) through integrin receptors on the cell surface [7]. This engagement and the force required to push the membrane forward is generated by vinculin and talin [8, 9]. Talin binds the integrin receptors and activates them, and promotes their interaction with ECM [10, 11]. Vinculin is then recruited to focal adhesion sites and serves as a link between Talin/integrin receptors and the actin cytoskeleton [9, 12].

Vinculin is a 117 kDa protein made up of three major domains – an N-terminal head (Vh), polyproline linker, and a C-terminal tail domain (Vt) [13]. Vinculin exists in an auto-inhibited state in which all the ligand-binding sites are masked by intramolecular interactions between the head and tail domains [14–17]. Vinculin activation results in conformational changes that disassociate head–tail interaction exposing the binding sites [16, 17]. Vinculin is found in neuronal growth cones and binds to talin and F-actin through its head and tail domains, respectively, and to several other actin-binding proteins [13, 18–20]. Vinculin has been shown to play a role in cell adhesion and motility in fibroblasts and PC12 cells. Vinculin null mice exhibit embryonic lethality

✉ Narendrakumar Ramanan
naren@iisc.ac.in

[1] Centre for Neuroscience, Indian Institute of Science, Bangalore 560012, Karnataka, India

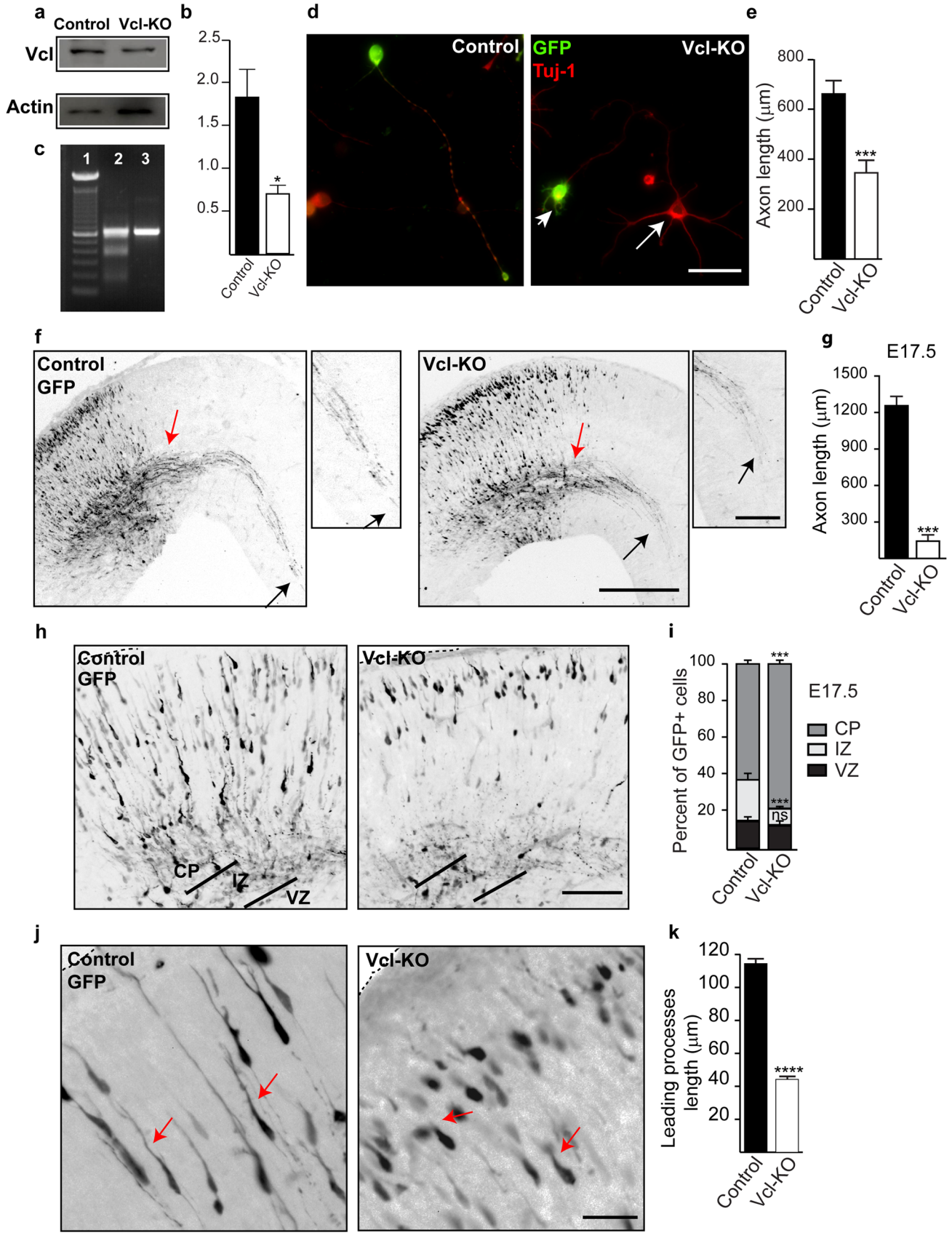
a
Control
Vcl-KO
Vcl
Actin
b
2.5
2.0
1.5
1.0
0.5
*
Control
Vcl-KO
c
1
2
3
d
Control
GFP
Tuj-1
Vcl-KO
e
800
600
400
200
Axon length (μm)
***
Control
Vcl-KO
f
Control
GFP
Vcl-KO
g
E17.5
1500
1200
900
600
300
Axon length (μm)
***
Control
Vcl-KO
h
Control
GFP
Vcl-KO
CP
IZ
VZ
i
100
80
60
40
20
Percent of GFP+ cells
***
***
ns
E17.5
CP
IZ
VZ
Control
Vcl-KO
j
Control
GFP
Vcl-KO
k
120
100
80
60
40
20
Leading processes length (μm)
****
Control
Vcl-KO

◂**Fig. 1** *Vinculin* deletion attenuated axon growth and enhanced neuronal migration. **a** Neonatal cortical neurons were transfected with a pair of single-guide RNAs (gRNA) targeting *Vinculin* along with Cas9 nickase and grown for 4 DIV. Western blot showing a reduction in vinculin expression in Vcl-gRNA transfected cells (Vcl-KO). Actin was used as the loading control. **b** Quantification of immunoblot signals from (a) ($n=3$). **c** T7E1 nuclease assay was done to detect indel mutations in the *vinculin* gene locus in the genomic DNA targeted by the sgRNAs. DNA gel showing the bands generated by digestion of mismatched DNA by T7E1 enzyme in Vcl-KO, while there was no digestion of control DNA (lane 1, 100 bp DNA marker; lane 2, Vcl-KO; lane 3, control). **d** Primary neocortical neurons were electroporated with either empty Cas9n-T2A-GFP plasmid or Vcl-gRNA-Cas9n-T2A-GFP construct. Cells were fixed at 4 DIV and immunostained for GFP for transfected neurons and β-III-tubulin (Tuj-1) to visualise neurites. Neurons expressing Vcl-gRNAs exhibited shorter neurites compared to control neurons. Non-transfected (arrow) and Vcl-gRNA expressing cells (arrowhead) are indicated. **e** Quantification of axon length from (d) ($n=100$ cells). **f** Neuronal progenitors were electroporated with either empty GFP (control) vector or Vcl-gRNA construct at E14.5 and analysed at E17.5. Deletion of vinculin attenuated axon growth in vivo. Black arrows indicate the axon terminals along the corpus callosum, while the red arrows indicate the position from where the axon length was quantified. The smaller panels show the magnified view of the axons, and the arrows point at the axon terminals. **g** Quantification of axon length from control and Vcl-KO brain sections. (3 sections/mouse, $n=3$ mice). **h** Embryos were electroporated at E14.5 with Vcl-gRNAs and analysed at E17.5. Vinculin deletion enhances neuronal migration during corticogenesis. **i** Quantification of the percentage of GFP^+ neurons in the cortical plate (CP), intermediate zone (IZ) and ventricular zone (VZ) shown in (h) (200 cells per mouse, $n=3$ mice). **j** Analysis at E17.5 also showed that deletion of *Vinculin* attenuates the length of leading processes as well. Arrows indicate the leading processes of migrating neurons. **k** Quantification of the length of leading processes from cortical plate neurons from (j) ($n=3$ mice. $n=100$ cells). Scale, 100 µm (d), 1 mm (f), 150 µm (inset in f), 400 µm (h), 100 µm (j). $^{***}P<0.001$, $^{****}P<0.0001$. ns, non-significant. Two-tailed Student's *t* test in (e), (g), (k). One-way ANOVA and Tukey's *post-hoc* test in (i)

at E10 with severe defects in the heart and neural tube development [21]. Vinculin-deficient fibroblasts showed poor adhesion to the substrate, less spreading, enhanced cell migration, and abnormal cytoskeletal dynamics [22–25]. Knockdown of vinculin or inhibition of its activity was shown to affect filopodia and lamellipodia dynamics and rate of neurite outgrowth in cultured PC12 cells and dorsal root ganglion (DRG) neurons [26, 27]. Our own findings suggested that vinculin may play an important role in axon growth in hippocampal neurons in vitro [28]. Despite these studies, the requirement for vinculin and the role of different functional domains of vinculin for neuronal migration and axon growth in vivo is poorly understood.

In this study, we show that vinculin deletion in cortical neurons affects neuronal migration and attenuates axon growth both in vitro and in vivo. Furthermore, we found that different domains of vinculin affect axon growth to different extents. Expression of a constitutively active vinculin significantly enhanced axon growth while the tail domain alone attenuated axon growth. Vinculin tail domain expression caused an abnormal and enlarged cell soma and highly branched neurites. Interestingly, abolishing vinculin-talin interaction did not affect neuronal migration and axon growth. The vinculin tail-induced branching phenotype was dependent on F-actin and Arp2/3 complex interactions. Thus, our findings provide novel insights into the role of vinculin in neuronal migration and axon growth.

Results

Vinculin is necessary for axon growth and proper neuronal migration

To understand the requirement of vinculin for axon growth, we first ablated vinculin in neocortical neurons using CRISPR/Cas9-mediated gene deletion (Fig. 1a-c). Neocortical neurons from postnatal day 1 (P1) mice were transfected with either empty Cas9n-T2A-GFP (Cas9-nickase) expressing plasmid or Cas9n-T2A-GFP plasmid along with a pair of guide RNAs (gRNAs) targeting exon 1 of *Vcl* gene and grown on poly-lysine- and laminin-coated coverglass. Neurons were fixed at 4 days post-electroporation and immunostained for β-III tubulin (Tuj-1) to label all neurites and GFP to identify transfected neurons. The control plasmid expressing neurons exhibited normal axon growth. In contrast, neurons expressing gRNAs targeting *Vcl* showed highly attenuated axon growth (Fig. 1d, e). This was consistent with our earlier finding in which shRNA-mediated knockdown of vinculin was found to attenuate axon growth in cultured hippocampal neurons [28]. Next, we asked whether vinculin deletion also affects axon growth in vivo. For this, we introduced vinculin gRNAs into neural progenitor cells by in utero electroporation (IUE) in embryonic day 14.5 (E14.5) embryos and analysed axon growth at E17.5. The vinculin gRNA expressing neurons exhibited much shorter axons compared to empty Cas9n-GFP plasmid (control) transfected embryos (Fig. 1f, g), suggesting that vinculin is necessary for axon growth. Vinculin null fibroblasts have been shown to exhibit increased cell mobility in cultures [22, 25]. We, therefore, analysed neuronal migration following vinculin deletion in the embryonic forebrain. During corticogenesis, neurons generated in the ventricular/subventricular zone migrate radially towards the pial surface and form distinct layers in an inside-out manner termed neocortical lamination [29]. We transfected control plasmid or Vcl sgRNAs into E14.5 embryonic forebrain by IUE and assessed cell migration three days later at E17.5. In control plasmid electroporated embryos, we found GFP^+ cells present in the cortical plate (CP), intermediate zone (IZ) and ventricular zone (VZ) (Fig. 1h, i). In contrast, most of the vinculin gRNA expressing neurons had migrated to the cortical plate, indicating a faster migration rate (Fig. 1h, i).

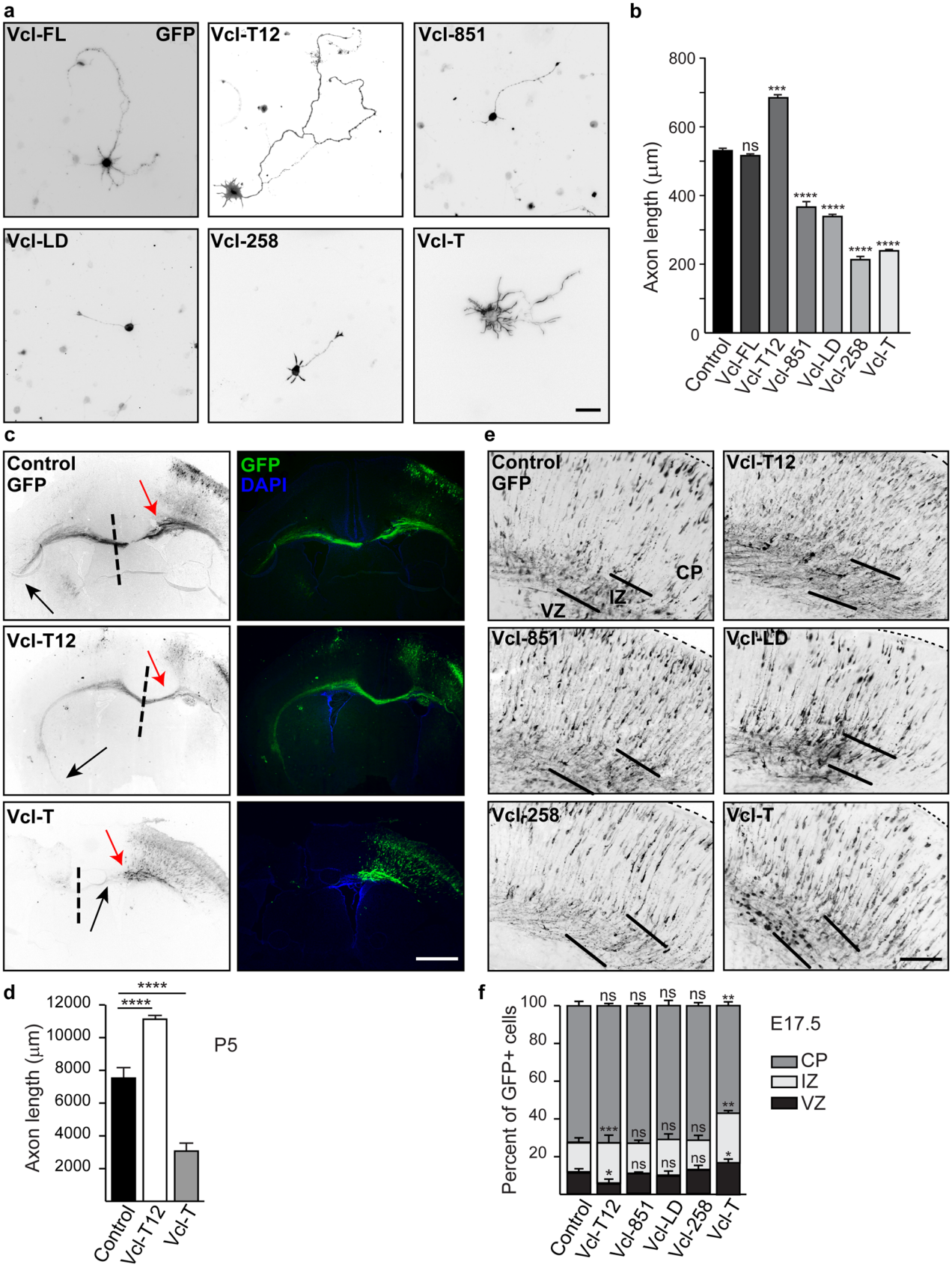
a
Vcl-FL
GFP
Vcl-T12
Vcl-851
Vcl-LD
Vcl-258
Vcl-T
b
Axon length (µm)
800
600
400
200
0
***
ns
****
****
****
****
Control
Vcl-FL
Vcl-T12
Vcl-851
Vcl-LD
Vcl-258
Vcl-T
c
Control
GFP
GFP
DAPI
Vcl-T12
Vcl-T
e
Control
GFP
Vcl-T12
CP
IZ
VZ
Vcl-851
Vcl-LD
Vcl-258
Vcl-T
d
Axon length (µm)
12000
10000
8000
6000
4000
2000
****
****
P5
Control
Vcl-T12
Vcl-T
f
Percent of GFP+ cells
100
80
60
40
20
ns
ns
ns
ns
**
***
*
ns
ns
ns
ns
ns
ns
**
**
*
E17.5
CP
IZ
VZ
Control
Vcl-T12
Vcl-851
Vcl-LD
Vcl-258
Vcl-T

◂**Fig. 2** Different requirements for the functional domains of vinculin for axon growth and cell migration in vivo and in vitro. **a** Primary neocortical neurons from P0.5 mouse pups were electroporated with different N-terminal GFP-tagged domain constructs of *Vinculin,* grown for 4 DIV and immunostained for GFP. Absence of either head and neck (Vcl-T), neck and tail (Vcl-258) or tail alone (Vcl-851) and PIP2-binding defective mutant (Vcl-LD) attenuated axonal growth, while the constitutively active vinculin (Vcl-T12) enhanced axon growth and the full-length (Vcl-FL) did not have any effect. **b** Quantification of axon length in neurons expressing different mutants of vinculin shown in (a) ($n = 250$–300 cells). **c** Neocortical progenitors in E14.5 embryos were transfected with the domain deleted constructs of vinculin by in utero electroporation (IUE). The pups were sacrificed at P5, and axons were visualised using anti-GFP immunostaining (green). The Vcl-T transfected neurons exhibited highly stunted axons compared to the control GFP neurons. In contrast, Vcl-T12 expression increased axon growth significantly. Black arrows indicate the axon terminals along the corpus callosum and the red arrows indicate the position from where the axon length was quantified. Dashed lines represent the longitudinal fissure separating the two cerebral hemispheres. **d** Quantification of axon length from (c) (3 sections/mouse, $n = 3$ mice). **e** Embryos were electroporated at E14.5 and harvested at E17.5. Brain sections were immunostained for GFP to visualise cell migration. **f** Quantification of the percentage of GFP + neurons in the cortical plate (CP), intermediate zone (IZ) and ventricular zone (VZ) from (e). More Vcl-T expressing neurons were seen in the intermediate and ventricular zones compared to control, indicating delayed migration, whereas Vcl-T12 + neurons showed faster migration compared to control. ($^{*}P = 0.0254$, Ctrl-Vcl-T12, $^{*}P = 0.0258$, Ctrl-Vcl-T; $n = 3$ mice, n = 200 cells/mouse). Scale, 100 µm (a), 2 mm (c), 400 µm (e). $^{**}P < 0.01$, $^{***}P < 0.001$, $^{****}P < 0.0001$. *ns* non-significant. One-way ANOVA and Tukey's *post-hoc* test in (b) and (f). Two-tailed Student's *t* test in (d)

Furthermore, we found that the vinculin gRNA expressing cortical plate neurons exhibited a shorter leading process compared to the control GFP^{+} neurons (Fig. 1j, k). Together, these findings suggest that vinculin deletion attenuates neurite growth and enhances cell migration in vivo.

Vinculin functional domains affect axon growth and cell migration differently

Vinculin has three major domains – head, neck and tail domains, through which it interacts with other actin-binding proteins, kinases and F-actin. But the requirements for these domains for axon growth and neuronal migration is poorly understood. To study this, we expressed several N-terminal GFP-tagged vinculin mutants in cultured neocortical neurons and assessed for axon growth at 4 days in vitro (DIV) [30–32] (Suppl. Figure 1). These mutants included vinculin full-length (Vcl-FL), vinculin N-terminal domain lacking the tail domain (Vcl-258, amino acids 1–258; Vcl-851, amino acids 1–851), vinculin tail domain (amino acids 881–1066) that binds actin (Vcl-T), a constitutively active form of vinculin (Vcl-T12) that has point mutations abolishing the head–tail interactions and a vinculin mutant that cannot bind PIP2 (Vcl-LD) [31, 33]. Expression of each of these mutants affected axon growth to varying extents (Fig. 2a, b). Vcl-FL expression did not increase axon growth any further compared to control plasmid transfected cells. However, Vcl-T12 expression significantly increased axon growth while the other mutants attenuated axon growth (Fig. 2b). We next asked whether Vcl-T12 also increases axon growth in vivo. For this, we electroporated embryos at E14.5 and analysed axon growth at P5. For comparison, we chose Vcl-T, which caused a severe attenuation of axon growth in cultured neurons. Similar to that seen in cultured cells, Vcl-T12 was able to increase axon growth in vivo compared to control GFP^{+} neurons. In contrast, Vcl-T neurons exhibited highly stunted axon growth (Fig. 2c, d). Together these findings suggest that the full-length vinculin is required for normal axon growth while constitutively active vinculin, which exists in an open conformation, can augment axon growth. On the other hand, Vcl-T expression appeared to have a dominant-negative effect on axon growth.

We next asked about the requirement for these domains for neuronal migration. We transfected the above vinculin mutants in E14.5 embryos by IUE and assessed cell migration at E17.5. We did not see any defects in cell migration when Vcl-258 and Vcl-851 were expressed as compared to control GFP transfected cells (Fig. 2e, f). However, when the constitutively active Vcl-T12 mutant was expressed, more GFP^{+} cells were seen in the intermediate zone (IZ) and less number in the ventricular zone (VZ). But there was no change in the number of cells in the cortical plate. In contrast, Vcl-T expressing cells showed delayed migration to the cortical plate with an increase in the number of cells in the ventricular zone (Fig. 2e, f). Together these findings indicated that lack of the vinculin tail domain (Vcl-258 and Vcl-851) does not affect neuronal migration, while vinculin tail domain expression severely delays cell migration from the ventricular zone/intermediate zone. Vcl-T12 appears to enhance migration from the intermediate zone compared to Vcl-T mutant, but not to the extent seen with vinculin deletion (Fig. 2e, f). Given this interesting phenotype observed with Vcl-T12 and Vcl-T mutants, we next asked how these mutants affected migration at a later time point. For this, we electroporated embryos at E14.5 and analysed cell migration at P5. The Vcl-T12 expressing neurons that were seen enriched in IZ at E17.5 have reached the upper layers of the cortex, and there was no significant difference compared to control GFP expressing cells. In striking contrast, a greater number of Vcl-T expressing neurons were still seen in the lower layers (VZ/IZ and layers 5/6) (Fig. 3a, b). We further confirmed the defect in neuronal migration using immunostaining for Cux1, which is specifically expressed in layers 2–4 in the neocortex [34]. We observed more Cux1^{+} cells in the lower layers in Vcl-T transfected embryos than those expressing control GFP (Fig. 3c, d). Interestingly, while analysing cell migration, we noticed that Vcl-T expressing neurons exhibited abnormal cell soma morphology. We analysed

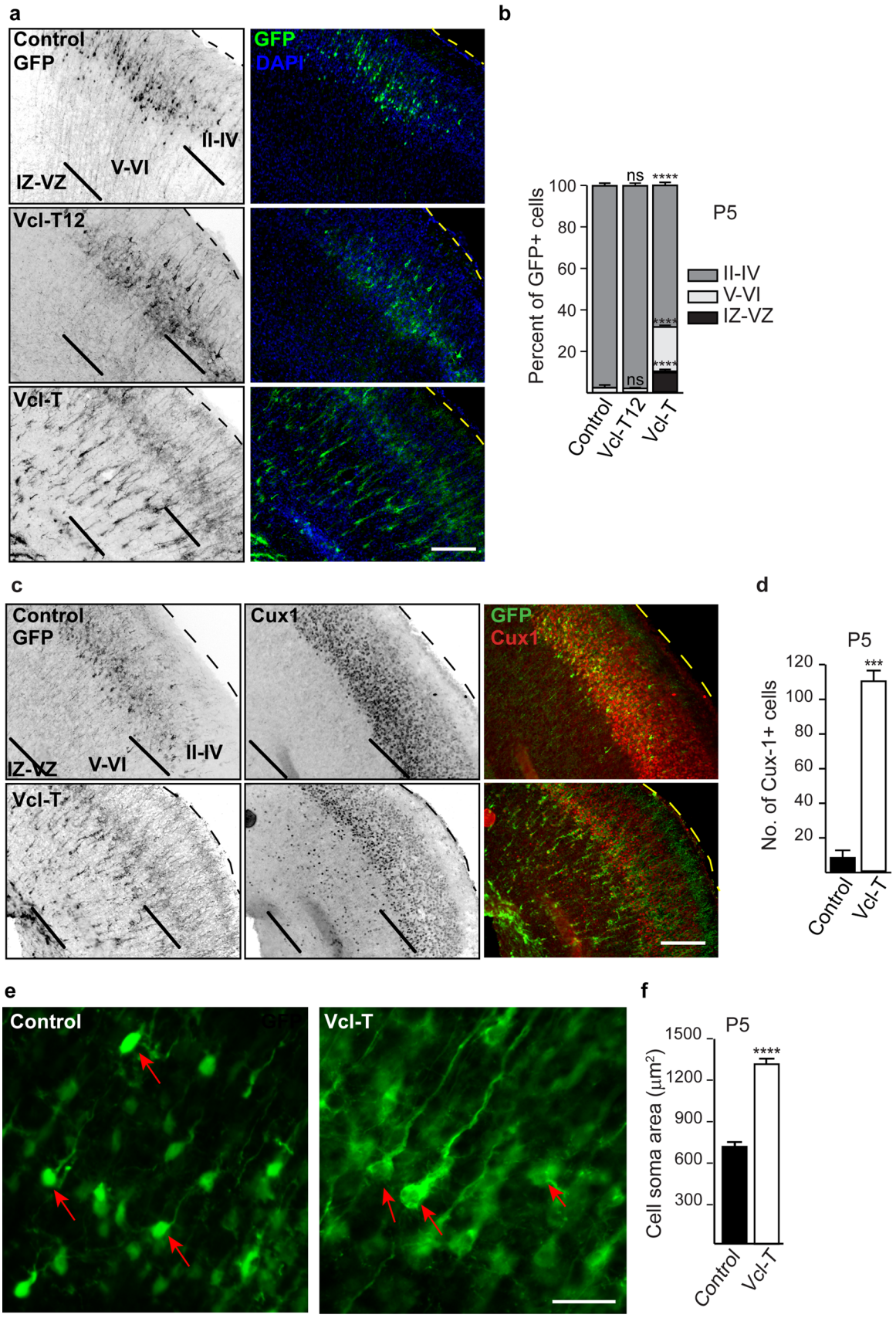
a
Control
GFP
II-IV
V-VI
IZ-VZ
Vcl-T12
Vcl-T
GFP
DAPI
b
P5
Percent of GFP+ cells
100
80
60
40
20
ns
****
ns
****
****
II-IV
V-VI
IZ-VZ
Control
Vcl-T12
Vcl-T
c
Control
GFP
IZ-VZ
V-VI
II-IV
Vcl-T
Cux1
GFP
Cux1
d
P5
No. of Cux-1+ cells
120
100
80
60
40
20
***
Control
Vcl-T
e
Control
Vcl-T
f
P5
Cell soma area (μm²)
1500
1200
900
600
300
****
Control
Vcl-T

◂**Fig. 3** Vcl-T expression affects neocortical lamination. **a** Representative images from the P5 cortex showing neuronal migration following electroporation of neocortical progenitors in E14.5 embryos with control GFP, GFP-Vcl-T12 or GFP-Vcl-T expression constructs. Vcl-T expressing neurons were still in the migratory phase even at P5, while Vcl-T12 expressing cells had migrated to the upper layers of the cortex. **b** Quantification of the percentage of GFP + neurons in different layers of cortex from (a) ($n = 3$ animals. $n = 200$ cells). **c** Embryos were electroporated at E14.5 with control GFP plasmid or Vcl-T and analysed at P5. Brain sections were immunostained for GFP and layer 2–4 specific marker, Cux1. In control sections, all $Cux1^+$ neurons had reached the upper layers as expected. In contrast, in the Vcl-T transfected embryos, many $Cux1^+$ neurons were seen occupying the lower layers, including around the ventricular zone/intermediate zone (VZ/IZ). **d** Quantification of the number of $Cux1^+$ cells in bottom layers of cortex (layers V & VI) and in IZ/VZ from (c) ($n = 3$ animals). **e** Representative images of neurons transfected with either empty GFP (control) or Vcl-T in vivo in E14.5 embryos. The Vcl-T expressing neurons exhibited larger and abnormal cell soma compared to control neurons. **f** Quantification of cell soma area from (e) ($n = 3$ animals. $n = 100$ cells). Scale, 400 µm (a), (c), 100 µm (e). $^{***}P < 0.001$, $^{****}P < 0.0001$. *ns* non-significant. One-way ANOVA and Tukey's *post-hoc* test in (b). Two-tailed Student's *t* test in (d), (f)

the area of neuronal soma and found that Vcl-T expressing cells had a much larger cell soma compared to control neurons (Fig. 3e, f).

Talin binding is dispensable for vinculin-dependent axon growth

Previous studies have shown that the interaction of vinculin with talin, a focal adhesion protein that binds to the integrin receptors, is important for mechanotransduction [35]. The amino acid alanine at position 50 in the vinculin N-terminal domain is critical for binding talin, and the alanine to isoleucine substitution (Vcl^{A50I}) abolishes this interaction [16, 32]. We generated GFP-tagged full-length mutant (GFP-Vcl-FL^{A50I}), GFP-Vcl-851^{A50I} and GFP-Vcl-258^{A50I} mutants and expressed them in cultured neocortical neurons. We did not observe any discernible difference in the levels of expression of these mutants (data not shown). Interestingly, we found that the GFP-Vcl-FL^{A50I} did not affect axon growth when compared to Vcl-FL and empty vector (Fig. 4a, b). Similarly, the GFP-Vcl-851^{A50I} and Vcl-258^{A50I} mutants did not exacerbate the attenuated axon growth phenotype caused by Vcl-851 and Vcl-258 mutants, respectively (Fig. 4b). We next asked whether talin binding is necessary for cell migration. For this, we compared cell migration at E17.5 following expression of Vcl-FL^{A50I} and control GFP. We did not observe any difference in cell migration when Vcl-FL^{A50I} was expressed (Fig. 4c, d). Together our observations suggested that either talin-binding to vinculin is dispensable for axon growth and neuronal migration or that the Vcl-A50I mutants do not exert a dominant-negative effect as seen with Vcl-T. It is also likely that other actin-binding proteins such as α-actinin, which has been shown to bind vinculin and integrins, compensates for the lack of talin binding [36, 37].

Vinculin tail domain induced excessive branching and enlarged cell soma

Since Vcl-T affected axon growth and migration, we sought to characterise further the effects of Vcl-T expression on neuronal morphology. First, we wanted to see whether the expression levels of the vinculin constructs were comparable. For this, we quantified the GFP fluorescence intensity of Vcl-T, Vcl-FL, and control (empty) plasmid in the cell soma at 4 days following transfection. We found that all constructs expressed to comparable levels (Suppl. Figure 2a). Next, we looked at neurite branching and, using Sholl analysis, quantified the number of primary neurites arising from the cell soma and the number of secondary branches arising from the primary neurites. The control GFP transfected neurons exhibited a single long axon and multiple dendrites that exhibited fewer branching. In contrast, Vcl-T increased both the number of primary and secondary neurites (Suppl. Figure 2b, c). We had earlier observed abnormal cell soma morphology of Vcl-T expressing neurons in vivo (Fig. 3e, f). We, therefore, asked whether this phenotype is also seen in cultured neurons. Neocortical neurons were transfected with Vcl-T or control GFP and grown in culture for 4 days. Cells were fixed and stained for rhodamine-conjugated phalloidin to label F-actin. We found that Vcl-T expressing neurons exhibited a larger cell soma indicating that Vcl-T expression increased cell spreading (Fig. 4e, f). This is in contrast to observations made in cultured fibroblasts, wherein, Vcl-T expression was shown to reduce focal adhesions resulting in a smaller cell area [30, 38].

Neocortical neurons in culture have been shown to exhibit a stereotypic pattern of growth [39]. Following plating, first, the neurons extend several filopodial and lamellipodial protrusions from the cell soma (stage 1), followed by extension of many neurites (stage 2). Next, one of these neurites grows rapidly to become the axon (stage 3), followed by dendritic growth (stage 4). We, therefore, asked how Vcl-T affected the early stages of neuronal growth. For this, primary neocortical neurons were transfected with Vcl-T or control GFP and cultured in vitro. Cells were fixed at 24 h and 48 h and analysed for the number of primary and secondary neurites and the length of the axon. At 24 h post-plating, the Vcl-T transfected neurons showed a greater number of primary neurites that also showed more branches (secondary neurites) with no significant difference in the length of the axon (Suppl. Figure 3a, b). At 48 h post-plating, the number of primary and secondary neurites remained higher in Vcl-T transfected neurons compared to control neurons (Suppl. Figure 3c, d). However, the length of the axon was shorter in Vcl-T expressing neurons compared to control (Suppl.

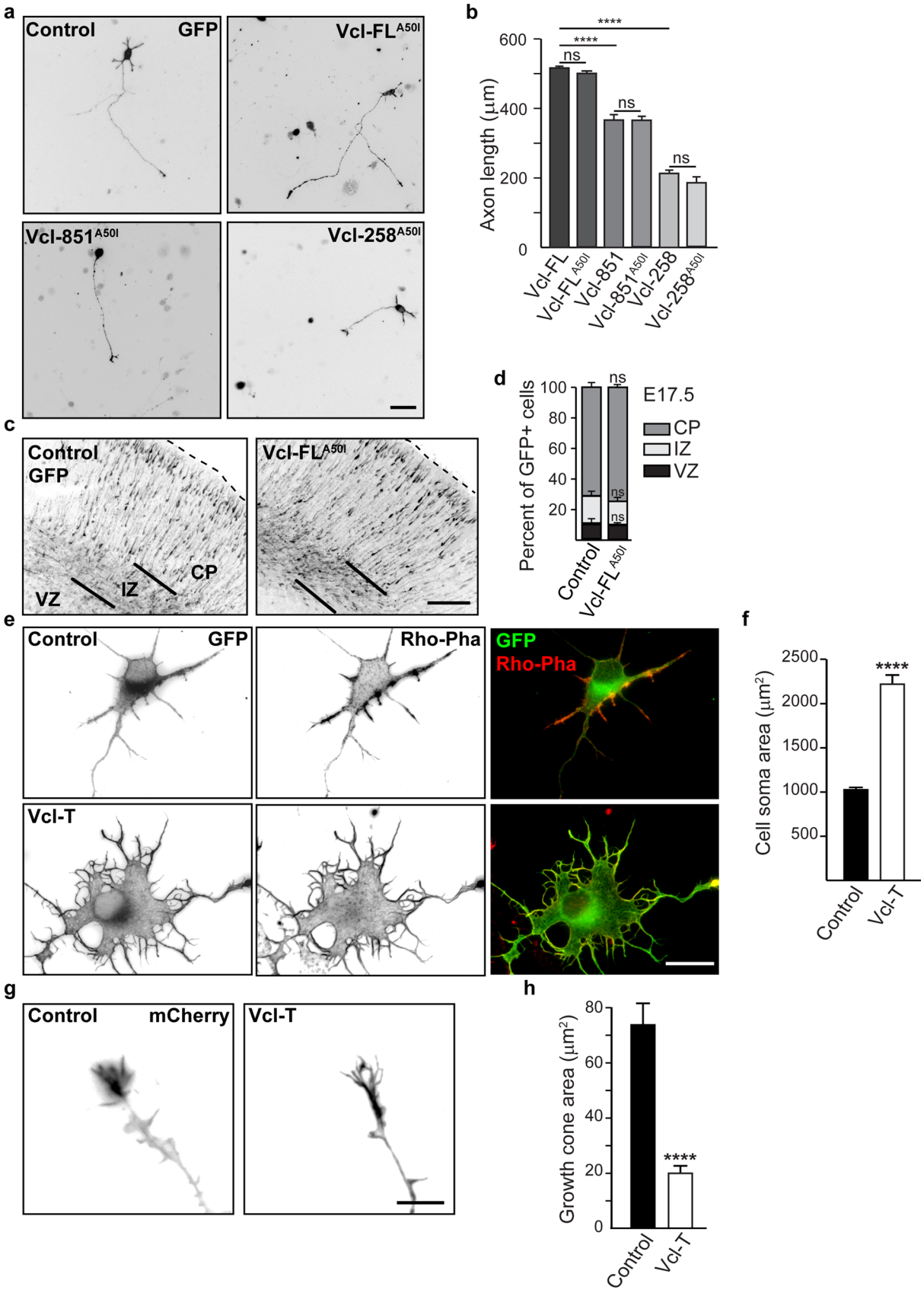
a
Control
GFP
Vcl-FL^A50I
Vcl-851^A50I
Vcl-258^A50I
b
Axon length (μm)
600
400
200
0
****
****
ns
ns
ns
Vcl-FL
Vcl-FL^A50I
Vcl-851
Vcl-851^A50I
Vcl-258
Vcl-258^A50I
c
Control
GFP
Vcl-FL^A50I
VZ
IZ
CP
d
Percent of GFP+ cells
100
80
60
40
20
ns
ns
ns
E17.5
CP
IZ
VZ
Control
Vcl-FL^A50I
e
Control
GFP
Rho-Pha
GFP
Rho-Pha
Vcl-T
f
Cell soma area (μm²)
2500
2000
1500
1000
500
****
Control
Vcl-T
g
Control
mCherry
Vcl-T
h
Growth cone area (μm²)
80
60
40
20
0
****
Control
Vcl-T

◂**Fig. 4** Interaction of talin with vinculin does not affect axonal growth and neuronal migration. **a** Primary neocortical neurons were electroporated with GFP-tagged vinculin constructs that contained the head domain but were defective in talin binding (Vcl-FL^{A50I}, Vcl-258^{A50I} and Vcl-851^{A50I}). Length of the axon was compared with the corresponding mutants having intact talin binding site (Vcl-FL, Vcl-258 and Vcl-851). **b** Quantification of axon length from (a). Abolishing talin-vinculin interaction did not affect axonal growth in vitro. ($n=200$ cells). **c** IUE was performed using control GFP, and Vcl-FL^{A50I} plasmids and the embryos were harvested at E17.5 to study migration. Inhibition of talin-vinculin interaction did not affect neuronal migration. **d** Quantification of the percentage of GFP^{+} neurons in the cortical plate (CP), intermediate (IZ) and ventricular zone (VZ) from (c) ($n=3$ animals. $n=200$ cells). **e** Representative images of neurons expressing either empty GFP (control) or Vcl-T plasmid at 4DIV. Neurons were immunostained for GFP and rhodamine-conjugated phalloidin (Rho-Pha) to visualise cell soma in vitro. Vcl-T expressing neurons had a wider spread of cell soma compared to control. **f** Quantification of the cell soma area in control and Vcl-T expressing neurons from (e) ($n=100$ cells). **g** Representative images from live imaging of control and Vcl-T expressing neurons co-transfected with LifeAct-mCherry to label actin. Vcl-T expression caused a smaller or collapsed growth cone morphology. **h** Quantification of the growth cone area in control and Vcl-T expressing neurons from (g) ($n=25$ cells). Scale, 100 µm (a), 400 µm (c), 50 µm (e), 10 µm (g). ****$P<0.0001$; ns, non-significant. One-way ANOVA and Tukey's *post-hoc* test (b and d). Two-tailed Student's *t* test (f), (h)

Figure 3c, d). Since a single longer neurite was not evident in Vcl-T expressing neurons, we wondered whether neuronal polarity was affected in these cells. We immunostained the cultures for the axon specific marker, Tau. We found that although shorter, the Vcl-T expressing neurons extended only one axon (Suppl. Figure 2a, b). Together, these findings suggested that although Vcl-T expression does not affect neuronal polarity, it attenuated axon growth and increased neurite branching from an early stage of neurite growth.

Vinculin is present in the leading edge of processes where it helps in binding to the substratum to promote migration [40]. The Vcl-T expressing neurons had shorter axons in vitro (Fig. 2a, b) and in vivo (Fig. 2c, d). Therefore, we asked whether growth cone morphology is affected in Vcl-T expressing neurons since improper growth cone can affect axon growth. For this, we analysed growth cone structure in the cultured neurons expressing Vcl-T and control GFP co-transfected with LifeAct-mCherry. We found that the area of the growth cone was smaller and appeared less spread out in Vcl-T compared to control GFP expressing neurons (Fig. 4g, h and supplementary movie 1–4).

Vcl-T expression has been shown to reduce focal adhesions in fibroblasts [30]. We wanted to know whether Vcl-T expression had a similar effect on focal adhesion (FA) in neurons and whether this could explain the enlarged cell soma and attenuated axon growth. For this, we transfected mouse cortical neurons with the empty (control) vector or Vcl-T construct and immunostained for GFP and focal adhesion kinase (FAK) to label transfected cells and focal adhesions, respectively. The expression and localisation of FAK in cell soma, axon and growth cone in control neurons were similar to that previously reported [41]. Interestingly, we did not observe any difference in the density (number of puncta per unit area) of FAK in cell soma (Suppl. Figure 4a, b) and growth cone (Suppl. Figure 4c, d) of neurons expressing Vcl-T when compared to control GFP transfected neurons suggesting that focal adhesion is not affected by Vcl-T expression. Together, these observations suggest that Vcl-T affects neuronal soma and growth cone motility and morphology, and this is not due to changes in the number of focal adhesions.

Vcl-T-mediated branching phenotype requires Arp2/3 activity and actin-binding

The attenuation of axon growth and the excessive branching phenotype caused by Vcl-T suggested that the vinculin tail domain affected actin dynamics and inhibited actin polymerisation [42]. The actin cytoskeleton binds to a large array of actin-binding proteins, which regulate the structural changes in actin, including polymerisation and nucleation. The actin-related protein 2/3 (Arp2/3) complex is an important actin nucleator that binds to existing actin filaments and causes branching of actin filaments and neurites [43–45]. We asked whether the neurite branching caused by Vcl-T expression is dependent on the Arp2/3 complex. We transfected neocortical neurons with Vcl-T or control GFP and cultured them in the presence of 25 nM of CK-666, a small molecule inhibitor of the Arp2/3 complex [46]. Inhibition of Arp2/3 complex completely suppressed the branching phenotype, and the number of primary and secondary neurites in Vcl-T expressing neurons were similar to that of control cells (Fig. 5a, b). However, inhibition of the Arp2/3 complex failed to reverse the attenuated axon length caused by Vcl-T and caused a further decrease in growth compared to Vcl-T expressing neurons (Fig. 5b). We next asked whether the localisation of proteins that regulate actin polymerisation is affected in the presence of Vcl-T since this could likely affect axon elongation. To this end, we immunostained neurons for the actin-severing protein, Cofilin. We did not observe any difference in the cofilin localisation in the cell soma (Suppl. Figure 5a, b) and growth cone (Suppl. Figure 5c, d) of Vcl-T transfected neurons when compared to control neurons. This suggested that the attenuated axon growth caused by Vcl-T expression is unlikely due to a change in the distribution of actin-filament regulatory proteins such as Cofilin and is likely due to altered interaction between actin and Vcl-T.

The vinculin tail domain binds F-actin and crosslinks it into actin bundles [20, 47]. Among several amino acid residues identified in the Vcl-T domain that binds to actin, the isoleucine 997 to alanine mutant (Vcl-T^{I997A}) was found to be the most impaired in actin-binding [48]. We generated Vcl-T^{I997A} mutant to determine the effect of abolishing

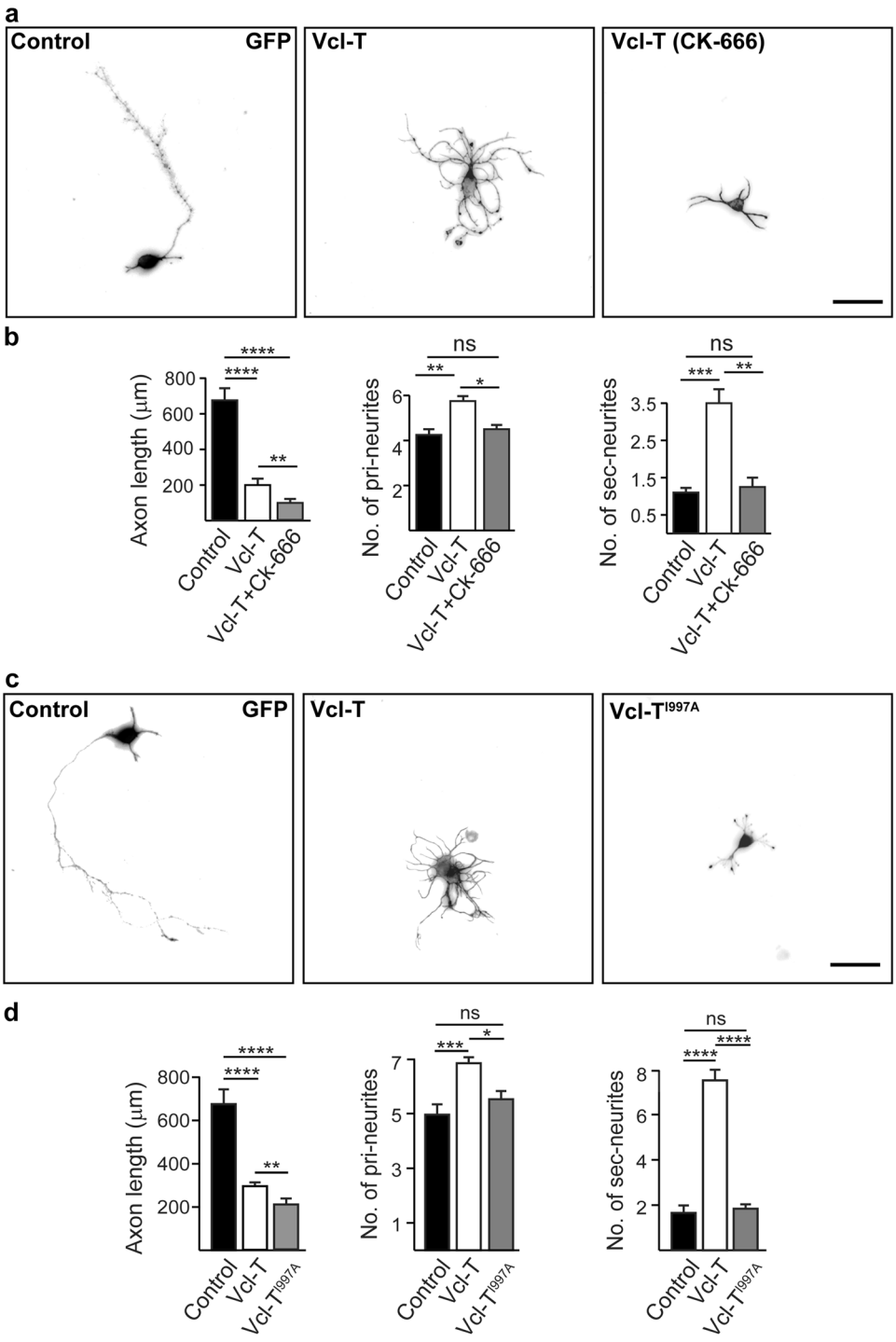

Fig. 5 Blocking the Arp2/3 complex reduces branching in Vcl-T neurons. Abolishing actin-Vcl-T interaction does not increase branching like Vcl-T but collapses the growth cone. **a** Representative images of neurons transfected with Vcl-T and treated either with DMSO (vehicle) or with 25 nM CK-666 (Arp2/3 complex inhibitor) dissolved in DMSO. Vcl-T neurons exhibited enhanced neurite branching, and this abolished in the presence of CK-666. **b** Quantification of axon length, number of primary and secondary neurites of neurons from (a) ($n = 100$ cells). **c** Neurons transfected with control, Vcl-T and Vcl-T defective in actin-binding (Vcl-T^{I997A}) constructs and immunostained for GFP after 4DIV. Abolishing interaction of Vcl-T with actin did not increase branching. **d** Quantification of axon length, number of primary and secondary neurites of neurons from (c) ($n = 300$ cells). Scale, 100 µm (a), (c). $^{**}P < 0.01$, $^{***}P < 0.001$, $^{****}P < 0.0001$; *ns* non-significant. Two-tailed Student's *t* test (b), (d)

actin-Vcl-T interaction on axon growth and neuronal morphology. Neocortical neurons expressing Vcl-T^{I997A} showed a decreased branching phenotype compared to Vcl-T expressing neurons, and the number of primary and secondary neurites were comparable to that of control neurons (Fig. 5c, d). But similar to that seen with Vcl-T expression, abolishing Vcl-T-actin interaction also attenuated axon growth (Fig. 5d).

We next asked whether abolishing actin-Vcl-T interaction affects cell soma phenotype. We found that the Vcl-T^{I997A} mutant did not cause any increase in cell soma area as seen in Vcl-T expressing neurons (Suppl. Figure 6a, b). This suggested that Vcl-T expression affected actin dynamics resulting in an enlarged soma, and abolishing this interaction with actin prevented enlargement of cell soma. We had earlier shown that Vcl-T caused a reduction in the area of the

growth cone, and this could be due to the ability of Vcl-T to bind the barbed ends of F-actin, preventing its polymerisation (Fig. 4g, h) [42]. We, therefore, asked whether abolishing actin-Vcl-T binding can prevent growth cone collapse and promote axon extension. For this, we transfected neurons with control GFP plasmid, Vcl-T or Vcl-T^{I997A}, along with LifeAct-mCherry to label actin. We found that the growth cone morphology was still collapsed in the absence of actin-binding. These results suggested that either Vcl-T binding likely recruits other actin-binding proteins that inhibit axon extension and affects growth cone or that the head and neck domains are required for normal axon growth (Suppl. Figure 6c, d and supplementary movie 5, 6).

Since abolishing actin-binding in Vcl-T (Vcl-T^{I997A}) was able to decrease Vcl-T-induced branching, we asked how the full-length vinculin that is deficient in actin-binding would function in neurons. For this, we generated a similar isoleucine 997 to an alanine point mutation in full-length vinculin (GFP-Vcl-FL^{I997A}) and expressed it in neurons. We found that Vcl-FL^{I997A} expression affected axon growth to a moderate but significant extent. However, it had no effect on branching (Suppl. Figure 6e, f).

Abolishing actin-Vcl-T binding does not affect neuronal migration

We had seen that Vcl-T impaired neuronal migration in vivo (Fig. 3a, b). We asked whether abolishing actin interaction with Vcl-T also affects migration. For this, we electroporated Vcl-T, Vcl-T^{I997A}, and control plasmids into E14.5 embryos and visualised neuronal migration three days later at E17.5. In contrast to the slower migration rate exhibited by Vcl-T expressing neurons, the Vcl-T^{I997A} neurons showed normal migration and were comparable to that seen in control embryos (Fig. 6a, b). We next looked at neuronal migration at a later time point (P5) following electroporation at E14.5. In control GFP transfection, the neurons had migrated to the upper layers as expected while the Vcl-T expressing neurons were stalled in the lower layers (Fig. 6c, d). However, the Vcl-T^{I997A} expressing neurons exhibited normal migration to the upper layers (Fig. 6c, d), indicating that abolishing actin-binding restores migration defect caused by Vcl-T. This was further confirmed by immunostaining for the upper layer marker, Cux1. In control GFP and Vcl-T^{I997A} transfected embryos, all Cux1^{+} cells were seen in layers 2 to 4 suggesting normal migration. However, in Vcl-T transfected embryos, many Cux1^{+} neurons were seen in the lower layers indicating retarded migration (Fig. 6e, f). Vcl-T expression was seen to impair axon growth in vivo (Fig. 2c, d). We asked whether the Vcl-T^{I997A} mutant also impairs the axon growth similar to Vcl-T. For this, we analysed the length of the axon along the corpus callosum at P5. In control GFP transfected brains, the axons from the transfected hemisphere had crossed over to the contralateral hemisphere, while in the Vcl-T transfected embryos, the axons were shorter, and very few crossed the midline (Fig. 7a, b). However, in Vcl-T^{I997A} transfected brains, the axons were longer and crossed the midline but were significantly shorter compared to control neurons (Fig. 7a, b). Together, these observations suggested that abolishing actin-Vcl-T binding restores normal migration compared to Vcl-T but not axon growth.

Vcl-T expression also resulted in an enlarged cell soma in vivo (Fig. 3e, f). We next asked whether inhibiting actin-Vcl-T binding also affects cell soma phenotype. For this, we measured the cell soma area of GFP^{+} neurons in the upper layers of the cortex at P5 in brain sections transfected with Vcl-T^{I997A} and compared the results with that of Vcl-T and control GFP expressing neurons. We found that the cell soma area of Vcl-T^{I997A} expressing neurons was comparable to that of control neurons (Fig. 7c, d), and this was similar to that observed in in vitro culture experiments (Suppl. Figure 4a, b). Together these results suggested that the defects in migration and abnormal morphology of neurons caused by vinculin tail domain were due to abnormal interaction with actin and that abolishing this interaction reverses both these defects in vivo and in vitro but not axon length.

Actin mobility is faster in neurons expressing vinculin tail domain

To understand the molecular mechanisms underlying the increased branching phenotype caused by Vcl-T, we studied actin mobility in cultured neurons. The Vcl-T^{I997A} expression data indicated that actin-binding is necessary for the branching phenotype. Vcl-T has been shown to affect actin dynamics by binding to the actin barbed ends and inhibiting its elongation [42]. To visualise actin dynamics in real-time, we co-electroporated neurons with LifeAct-mCherry along with a control GFP or Vcl-T construct. LifeAct, the first 17 amino acids of actin-binding protein 140 from *S. cerevisiae*, binds to actin filaments without modifying its function [49]. mCherry was tagged to LifeAct for visualisation of actin in cells. To study the behaviour of actin in neurons, we photobleached mCherry in a small region close to the edge of the axon by using a high-power laser of 561 nm wavelength and monitored fluorescence recovery over time (FRAP). The fluorescence recovery was fit as a single exponential function of time, and half-time of recovery and mobile fraction was calculated from the curve fitting (Fig. 7e-g). In Vcl-T expressing neurons, there was a recovery of the higher mobile fraction of LifeAct ($0.7655 +/- 0.06361$) when compared to the mobile fraction of control cells ($0.3071 +/- 0.03738$) (Fig. 7f). We also observed a significant increase in t-half of recovery in the presence of Vcl-T (3227 ms +/− 647.2 ms) compared to control

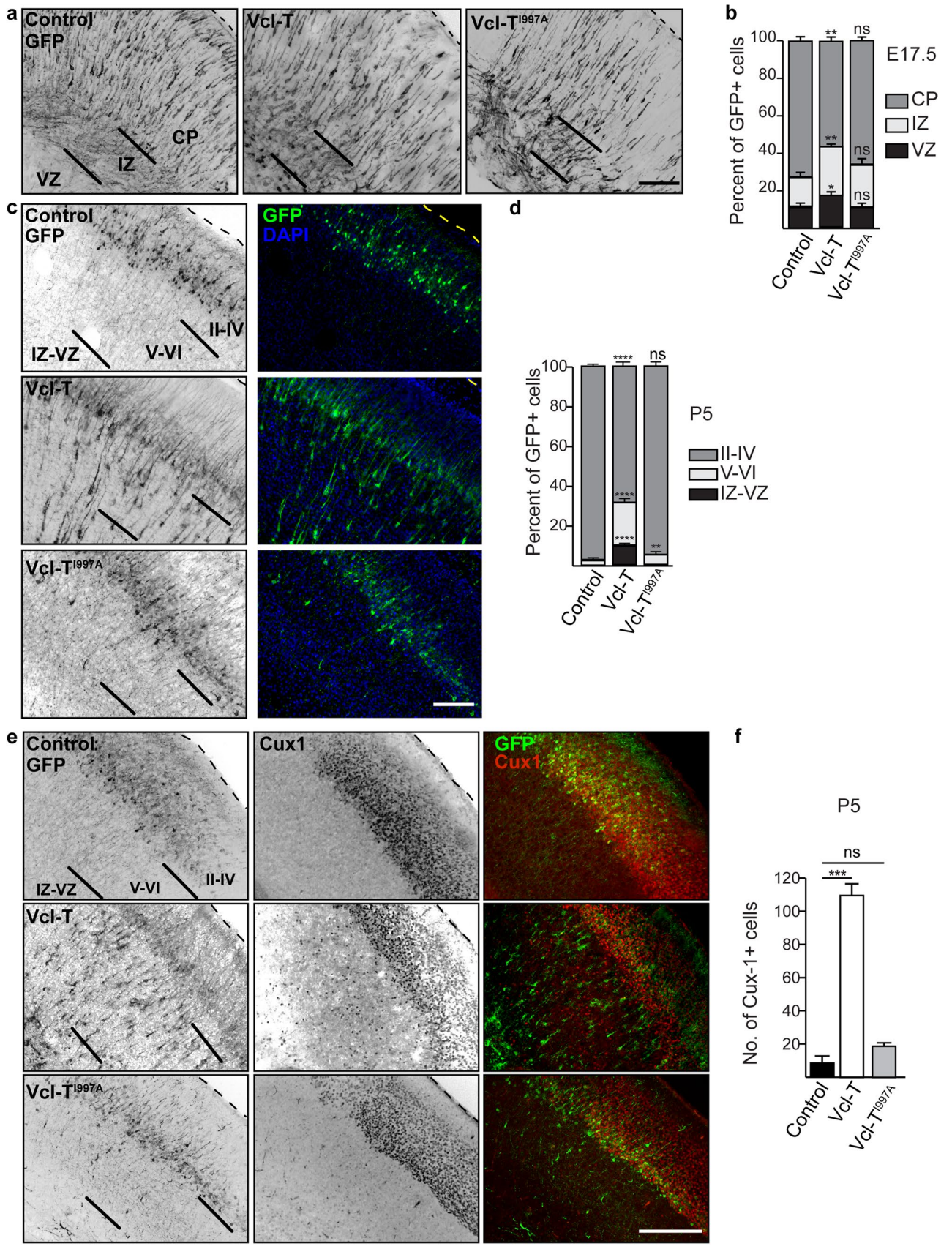
a
Control
GFP
Vcl-T
Vcl-T^I997A
CP
IZ
VZ
b
E17.5
Percent of GFP+ cells
100
80
60
40
20
**
ns
**
*
ns
ns
CP
IZ
VZ
Control
Vcl-T
Vcl-T^I997A
c
Control
GFP
GFP
DAPI
II-IV
IZ-VZ
V-VI
Vcl-T
Vcl-T^I997A
d
P5
Percent of GFP+ cells
100
80
60
40
20
****
ns
****
****
**
II-IV
V-VI
IZ-VZ
Control
Vcl-T
Vcl-T^I997A
e
Control
GFP
Cux1
GFP
Cux1
IZ-VZ
V-VI
II-IV
Vcl-T
Vcl-T^I997A
f
P5
No. of Cux-1+ cells
120
100
80
60
40
20
ns
***
Control
Vcl-T
Vcl-T^I997A

◂**Fig. 6** Abolishing actin-Vcl-T interaction does not affect neuronal migration. **a** Representative images of brain sections from E17.5 embryos following electroporation at E14.5 with control, Vcl-T and Vcl-T^{I997A} constructs. Abolishing actin-Vcl-T interaction does not delay neuronal migration like Vcl-T. **b** Quantification of the percentage of GFP^+ neurons in the cortical plate (CP), intermediate zone (IZ) and ventricular zone (VZ) from (a) ($n=3$ animals. $n=200$ cells). **c** Analysis at postnatal day 5 (P5) also showed almost no migration defect when actin-Vcl-T interaction is abolished. **d** Quantification of the percentage of GFP^+ neurons in different layers of cortex and in IZ/VZ from (**c**) ($n=3$ animals. $n=200$ cells). **e** Analysis of cortical lamination using Cux1 immunostaining shows normal migration of upper-layer neurons when actin-Vcl-T interaction is abolished. **f** Quantification of the number of $Cux1^+$ cells in the bottom layers of cortex (layer V–VI) and in IZ/VZ from (**e**) ($n=3$ animals). Scale, 400 µm (a), (c), (e). $^{**}P<0.01$, $^{***}P<0.001$, $^{****}P<0.0001$; ns, non-significant. One-way ANOVA and Tukey's *post-hoc* test in (**b**), (**d**), (**f**)

(941.5 ms +/− 171.0 ms) (Fig. 7e). This increase in mobile fraction could be due to either an increase in actin pool or impaired F-actin dynamics (actin treadmilling). Interestingly, neurons expressing the Vcl-T^{I997A} mutant, which is defective in actin-binding, showed mobile fraction recovery (0.3268 +/− 0.03837) and t-half (1139 ms +/− 206.2 ms) of actin comparable to that of control neurons (Fig. 7f, g).

To further characterise the effect of Vcl-T on actin mobility, we expressed Vcl-T along with mEOS3.2-LifeAct [50]. Using photoactivation properties of mEOS3.2, we performed single-particle tracking based photoactivation localisation microscopy on LifeAct in transfected cells. A high-resolution intensity map and single-particle trajectories were generated for each neuron (Fig. 7h). Instantaneous diffusion coefficient (D) and mean squared displacement (MSD) were calculated and used to estimate diffusion dynamics and confinement of the LifeAct molecules. The trajectories displayed a wide range of diffusion coefficient, and a significant difference in the distribution of logarithmic values of diffusion coefficient was observed, indicating that mEOS3.2-LifeAct was more mobile in the presence of Vcl-T (Fig. 7i). In presence of Vcl-T, instantaneous mEOS3.2-LifeAct showed increase in diffusion coefficient (0.2570 μm^2/sec, IQR: 0.1012–0.5867 μm^2/sec) when compared to control (0.1749 μm^2/sec, IQR: 0.06114–0.4980 μm^2/sec) after pooling all the trajectories obtained (Fig. 7k). To rule out the possibility of a cell-to-cell variation in diffusion coefficient, we compared the median diffusion coefficient from all cells extracted individually and found the difference to be significant (Fig. 7l). These values were consistent with the pooled analysis. The average MSD of LifeAct saturated with time in both conditions indicating confined diffusion in both cases. However, the saturation values of LifeAct in the presence of Vcl-T were higher than the control, indicating lesser confinement compared to control (Fig. 7j). This was also validated by a significant difference in the area under the curve for MSD, for the average MSD curves generated for each cell (Fig. 7m). Together these observations confirm that the actin molecules became more mobile upon vinculin tail domain expression.

Discussion

Actin cytoskeletal changes are important for proper neuronal migration, neurite outgrowth and axon extension, which are critical for normal circuit formation and function. This is the first study to report critical roles for the actin-binding protein vinculin in neuronal migration in vivo and in axon growth in vitro and in vivo. Although full-length vinculin is required for optimal axon growth, the mutants used in this study provide novel insights into the role of the functional domains of vinculin. The constitutively active vinculin greatly enhanced axon growth both in vitro and in vivo. Preventing vinculin-talin binding did not affect migration and axon growth, indicating that this interaction is dispensable for these vinculin-dependent functions, in contrast to that seen in fibroblasts. Interestingly, the vinculin tail domain caused increased neurite branching and cell soma size while attenuating axon length, and this was reversed by abolishing vinculin interaction with Arp2/3 complex and actin. Our results suggest that vinculin's interaction with actin is important for mediating neuronal migration and axon growth.

Given the importance of vinculin in focal adhesion formation and mechanotransduction, surprisingly little is known about its role in neuronal development. Vinculin null mutants exhibited embryonic lethality and died before E10, demonstrating an essential requirement for vinculin for mouse development [21]. Previous studies have shown that reducing vinculin expression by RNA interference or focal inactivation of vinculin resulted in unstable filopodia and lamellipodia in cultured PC12 cells and DRG neurons [26, 27]. Our results show that full-length vinculin is required for normal cell morphology and proper axon growth. Vinculin deletion caused a significant reduction in axon growth both in vitro and in vivo, and this was consistent with our previous in vitro observations [28]. Expression of different domain-deleted mutants suggested that these mutants exhibited a dominant-negative effect on axon growth to varying extents, but the expression of vinculin head (Vcl-258) or tail domains (Vcl-T) alone caused the most reduction. However, Vcl-T expression alone resulted in an abnormal branching phenotype. Expression of wild-type vinculin did not further augment normal axon growth in neurons, and this is consistent with the observations that vinculin exists in an auto-inhibited state and requires a conformational change in its structure to become active [16, 17]. Interestingly, expression of Vcl-T12 mutant, which is relieved of this auto-inhibition and is constitutively active [31], significantly enhanced axon growth. This also raises an interesting question of whether

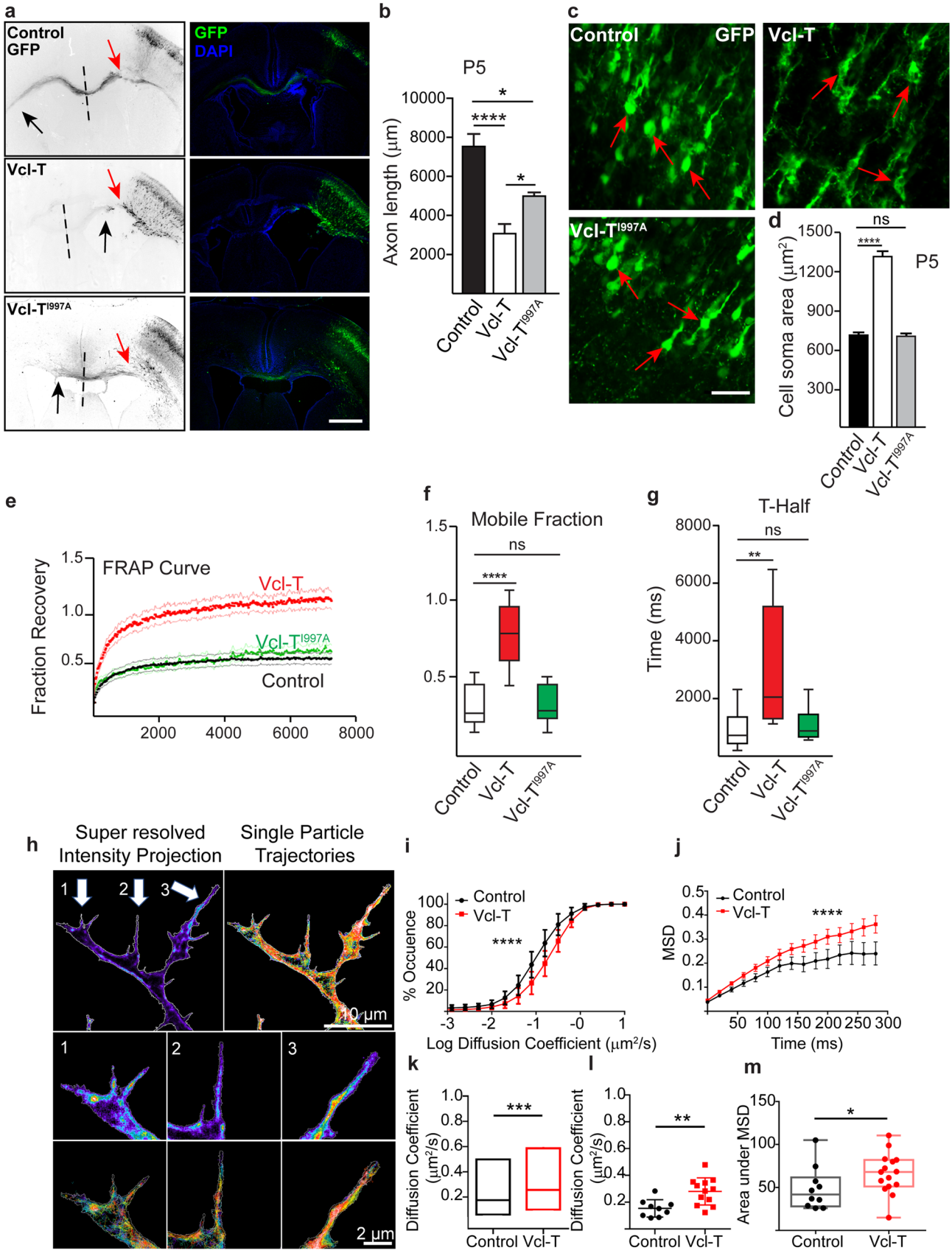
a
Control
GFP
GFP
DAPI
Vcl-T
Vcl-T^I997A
b
P5
Axon length (μm)
10000
8000
6000
4000
2000
*
****
*
Control
Vcl-T
Vcl-T^I997A
c
Control
GFP
Vcl-T
Vcl-T^I997A
d
Cell soma area (μm²)
1500
1200
900
600
300
ns
****
P5
Control
Vcl-T
Vcl-T^I997A
e
FRAP Curve
Fraction Recovery
1.5
1.0
0.5
Vcl-T
Vcl-T^I997A
Control
2000
4000
6000
8000
f
Mobile Fraction
1.5
1.0
0.5
ns
****
Control
Vcl-T
Vcl-T^I997A
g
T-Half
Time (ms)
8000
6000
4000
2000
ns
**
Control
Vcl-T
Vcl-T^I997A
h
Super resolved Intensity Projection
Single Particle Trajectories
1
2
3
10 μm
1
2
3
2 μm
i
% Occuence
100
80
60
40
20
Control
Vcl-T
****
-3
-2
-1
-0
1
Log Diffusion Coefficient (μm²/s)
j
MSD
0.5
0.4
0.3
0.2
0.1
Control
Vcl-T
****
50
100
150
200
250
300
Time (ms)
k
Diffusion Coefficient (μm²/s)
1.0
0.8
0.6
0.4
0.2
***
Control
Vcl-T
l
Diffusion Coefficient (μm²/s)
1.0
0.8
0.6
0.4
0.2
**
Control
Vcl-T
m
Area under MSD
150
100
50
*
Control
Vcl-T

◂**Fig. 7** Vcl-T expression increases actin mobility in vitro. **a** Representative images of brain sections electroporated with control, Vcl-T and Vcl-T^{I997A} constructs. Vcl-T^{I997A} defective in actin-binding has stunted axon similar to Vcl-T. Black arrows indicate the axon terminals along the corpus callosum and the red arrows indicate the position from where the axon length was quantified. Dashed lines represent the longitudinal fissure separating the two cerebral hemispheres. Scale, 2 mm. **b** Quantification of the length of axons from (a) (3 sections/mouse, n = 3 mice). *$P = 0.0193$, Vcl-T-Vcl-T^{I997A}; *$P = 0.0170$, Ctrl-Vcl-T^{I997A}; ****$P = 0.0001$, Ctrl-Vcl-T (One-way ANOVA). **c** Representative images of brain sections showing cell soma morphology of neurons expressing control GFP, Vcl-T and Vcl-T^{I997A}. Vcl-T expressing neurons exhibited abnormal soma (arrows) compared to control and Vcl-T^{I997A} expressing neurons. Scale, 100 µm. **d** Quantification of neuronal cell soma area from (c) ($n = 3$ animals. n = 100 cells). ****$P < 0.0001$; ns, non-significant (One-way ANOVA). **e–g** Neurons were transfected with control GFP, Vcl-T or Vcl-T^{I997A} along with LifeAct-mCherry to visualise actin. Fluorescence recovery curve (**e**), mobile fractions (**f**) and half-time (**g**) of recovery of fluorescence of LifeAct-mCherry after FRAP of neurons, showing that neurons expressing Vcl-T have a higher mobile fraction and higher t-half of actin compared to control neurons. Abolishing actin-Vcl-T interaction (Vcl-T^{I997A}) reduces the mobile fraction and t-half to normal levels. ($n = 10$ cells). **$P < 0.01$, ****$P < 0.0001$; ns, non-significant. **h–m** Single-particle tracking of mEOS3.2-LifeAct in control and Vcl-T expressing neurons. **h** Representative super-resolution intensity map reconstructed from single-molecule localisation (left) and single-particle trajectories (right) generated from neurons expressing mEOS3.2-LifeAct. White arrows indicate the extensions of the neurite. Scale, 10 µm. The regions marked by arrows are represented below. For each region indicated by the arrow, the magnified super-resolution intensity map (SR) and single-particle trajectories (SPT) for the same region are shown. Scale, 2 µm. **i** Normalised cumulative distribution of logarithmic values of the instantaneous diffusion coefficient of the generated tracks (Mean +/− SEM). ****$P < 0.0001$ (Kolmogorv-Smirnov test). **j** Plot of average mean squared displacement (MSD) of all trajectories above 6 frames for control and Vcl-T. ****$P < 0.0001$ (Wilcoxon matched-pairs signed-rank test). **k** Pooled values of the instantaneous diffusion coefficient of all the detected trajectories from control and Vcl-T (median, IQR). ***$P = 0.0002$ (Unpaired t test). **l** Distribution of median diffusion coefficients of each neuron compared across the conditions. **$P = 0.0039$ (Unpaired t test). **m** Distribution of the area under the curve for average MSD for trajectories obtained from each cell of control versus Vcl-T. *$P = 0.0469$ (Mann–Whitney test)

vinculin activation can promote axon growth on inhibitory substrates and also raises the possibility that inhibitory substrates could likely affect axon growth by blocking vinculin-dependent actin dynamics.

Focal adhesions (FA) and cell migration are very closely related, and cells that have slower migration exhibit increased FA-ECM interaction [51, 52]. This is evident in vinculin null cells, which have smaller FA, spread less and exhibit faster migration [22, 25]. Vinculin interacts with many other actin-binding and focal adhesion proteins, including paxillin, α-actinin, α-catenin, PIP2, VASP and Arp2/3 through its head, neck and tail domains [13, 40, 53]. Vinculin helps in cell spreading, and these functional domains are differently required for FA formation [30, 54]. Previous studies have shown that Vcl-T expression reduced the number of FAs in fibroblasts while Vcl-258, Vcl-851 and Vcl-T12 increased the size and number of FAs [30, 55]. Correspondingly, Vcl-258, Vcl-851 and Vcl-T12, which stabilised FAs, reduced cell migration rates [55]. Therefore, it was expected that the mutant vinculins that increase FA formation would exhibit slower neuronal migration while Vcl-T, similar to vinculin null cells, which forms poor FAs, will exhibit faster migration. However, we found that Vcl-T alone caused a delay in neuronal migration and affected cell soma and growth cone morphologies, whereas Vcl-258 and Vcl-851 expressing neurons exhibited normal morphology and migration rates compared to control neurons. But we did not observe any significant difference in the number of focal adhesions in Vcl-T expressing neurons compared to control neurons following immunostaining for focal adhesion kinase. Interestingly, Vcl-T12 enhanced cell migration but no discernible deficits in soma morphology.

Vinculin is known to interact directly with talin, and this is important for engagement with the integrins at the cell surface and for generating the mechanotransduction force necessary for cell protrusion and growth [13, 56]. This interaction is known to occur through alanine 50 residue in the head domain of vinculin since the Vcl-A50I point mutant has been shown not to bind talin [16, 30]. We found that the expression of Vcl-FL^{A50I} mutant that cannot bind talin did not affect both neuronal migration and axon growth. Furthermore, the Vcl-851^{A50I} mutant did not exacerbate the decrease in axon length caused by Vcl-851 expression. Together, these observations suggest that talin binding is likely dispensable for these vinculin-dependent processes. It is also possible that Vcl-A50I mutants used in this study do not exert a dominant-negative effect on axon growth as seen for the other mutants or that α-actinin binds vinculin to mediate migration and axon growth via a talin-independent process.

Among the various mutants, Vcl-T expression alone caused a striking increase in neurite branching, and this was reversed by abolishing interaction of the tail domain with actin or by inhibiting the Arp2/3 complex. Vcl-T has been shown to bind the barbed end of F-actin and to the side chain of actin filament [42]. This binding to the barbed end inhibits actin polymerisation and decreases actin association and dissociation [42]. The stalled neurite extension allows binding of the Arp2/3 complex to the actin filament, causing branching. This entire process appears to continue every few distances of growth, resulting in highly branched but shorter neurites. This is supported by our observation that pharmacological inhibition of Arp2/3 complex or abolishing actin-Vcl-T binding prevented this excessive branching phenotype but could not restore axon length. Attenuated axon growth caused by Vcl-T could be due to the altered distribution of proteins that regulate actin filament formation. We did not find any difference in the number of cofilin puncta

in Vcl-T expressing neurons when compared to control neurons. This indicated that Vcl-T affects axon elongation through its interaction with actin and not by affecting the distribution of actin-filament regulating proteins. Furthermore, using FRAP, we observed that the fluorescence recovery was around 30% in control cells while the recovery was nearly 100% in Vcl-T expressing neurons. Analysis of the mobile fraction from the recovery curve showed that Vcl-T expressing neurons had a higher amount of mobile fraction of actin compared to control neurons. Furthermore, single-particle tracking based photoactivation localisation microscopy of LifeAct-mEOS revealed that actin was more mobile in Vcl-T expressing neurons compared to control cells. These observations suggested that there is an increase in the pool of F-actin, which was more mobile in the presence of Vcl-T.

Materials and methods

Animals

For all experiments, C57Bl/6 J mice (Jax Stock Number #000,664 – internal breeding) were used. 6 to 12 weeks old mice were housed in individually ventilated cages (Techniplast, Italy) under conventional conditions (23 ± 2 °C, relative humidity 50 ± 10%, 12-h light/dark cycle) and had ad libitum access to food and water. The presence of a vaginal plug following mating was considered as E0.5. Neonatal pups (P1–P3) of both sexes were used for isolating primary cortical neurons. All procedures in this study were performed according to the rules and guidelines declared in the Compendium of CPCSEA 2018 by the Committee for the Purpose of Control and Supervision of Experimental Animals (CPCSEA), Ministry of Environment, Forest and Climate Change, India. The research protocol was approved by the Institutional Animal Ethics Committee (IAEC) of the Indian Institute of Science (Project No. CAF/Ethics/516/2016), allowing the use of animals for in vitro and in vivo studies.

Constructs

Sequences of guide RNAs (gRNAs) for deleting the vinculin gene was selected using DeskGen software (www.deskgen.com), and two gRNAs that bind to flanking regions of translational start site were chosen. The chosen gRNA sequences are as follows: Vcl-gRNA-1, 5'-GCG TACGATCGAGAGCATCC-3' and Vcl-gRNA-2, 5'-GCT AGCGGGGCGGCGTACCG-3'. The gRNAs were first individually cloned into the pX330-U6-BB-CBh-hSpCas9 plasmid (Addgene No: 42230) using the BbsI sites. These two gRNAs were then subcloned into pSpCas9n(BB)-2A-GFP plasmid (pX461; Addgene No: 48140). We made use of Cas9 nickase (Cas9n) to decrease any potential OFF-target effects. The resultant vector was named pX461-Vcl-sg1 + 2–Cas9n-2A-GFP. pSpCas9n(BB)-2A-GFP (PX461) and pX330-U6-Chimeric_BB-CBh-hSpCas9 were a gift from Feng Zhang (Addgene plasmid # 48,140, 42,230; http://n2t.net/addgene:48140; RRIDs: Addgene_48140, Addgene_42230).

The mouse *Vcl*-encoding gene (Vcl-FL) was amplified from cDNA synthesised from whole-brain mRNA. Vcl-FL^{A50I} was generated from Vcl-FL by mutating the alanine residue at 50th position to isoleucine using site-directed mutagenesis (SDM). Vcl-FL^{I997A} was generated from Vcl-FL by mutating isoleucine residue at 997th position to alanine using SDM. Vcl-LD was generated from Vcl-FL by mutating 1060th residue from arginine to glutamine and residue at 1061st from lysine to glutamine by using SDM. Vcl-258 was amplified from full-length vinculin by using the following primers: Forward 5'-CTTGAATTC GATGCCGGTGTTTCACACG-3' and Reverse 5'-CGG GGTACCCCAGGCGTCTTCATCCC-3'. Vcl-258^{A50I} was generated from Vcl-258 by mutating alanine residue at 50th position to isoleucine using SDM. Vcl-851 was amplified from full-length vinculin using the following primer: Forward, 5'-CTTGAATTCGATGCCGGTGTT TCACACG-3' and Reverse, 5'-CGCGGTACCCTCTTC TGGTGGTGGGG-3'. Vcl-851^{A50I} was generated from Vcl-851 by mutating alanine residue at 50th position to isoleucine using SDM. Vcl-T12 was generated by mutating residues 974th from glutamate to alanine, 975th from lysine to alanine, 976th from arginine to alanine and 978th from arginine to alanine from full-length vinculin by using SDM. Vcl-T was amplified from Vcl-FL by using these primers: Forward 5'-CTTGAATTCGAAGGATGAAGA GTTCCCTG-3' and Reverse 5'-CGCGGATCCCTGGTA CCAGGGAGTCTTTC-3'. All these clones were generated in the pCAG-C1 vector. pCAG-C1 was generated from the pEGFP-C1 vector by replacing the CMV promoter with CAG promoter from pCAGEN, a gift from Connie Cepko (Addgene plasmid # 11,160; http://n2t.net/addgene:11160; RRID: Addgene_11160). Vcl-T^{I997A} clone was generated from Vcl-T by site-directed mutagenesis of the 997th amino acid residue from isoleucine to alanine. LifeAct-mCherry was a gift from Dr. Paul Bridgman, Washington University School of Medicine, St. Louis, MO. mEos3.2-C1 was a gift from Michael Davidson & Tao Xu (Addgene plasmid # 54,550; http://n2t.net/addgene:54550; RRID: Addgene_54550). Vcl-T-mEOS3.2-LifeAct was generated by sub-cloning a Vcl-T-T2A fragment in the mEOS3.2-LifeAct plasmid.

Site-directed mutagenesis

Complementary primers of 30–40 bp were designed with the mutation site in the middle of the sequence, and 50 ng of template DNA was used along with 25 pmol each of the mutant primers. 2 min extension time for every 1 kb of template length was used. PCR was for a total of 18 cycles, and the following cycling conditions were used: 95 °C for 3 min; 68 °C for (2 min/kb); 18 cycles; 72 °C for 10 min; end at 4 °C. The reaction mixture was digested with DpnI enzyme to remove template DNA, and ligation was set with T4DNA ligase for 1 h at room temperature. A small aliquot of the ligation reaction was transformed into DH10B competent cells, and transformants were selected on LB + antibiotic plates. The site-directed mutation was confirmed by DNA sequencing of both strands of at least 2 independent clones.

T7E1 endonuclease assay

Primary cortical neurons were transfected with gRNA expressing construct (pX461-Vcl-sg1 + 2–Cas9n-2A-GFP) or empty Cas9n-GFP construct (pSpCas9n(BB)-2A-GFP). Genomic DNA was isolated 4 days post-transfection, and 10 ng of DNA was used to PCR amplify a 600 bp region flanking the gRNA target site using the following primers: forward, 5'-CAATAGGAGCCACAGTCCGG- 3' and reverse, 5'-GCCCCAAGGCAGGATTTCTC-3'. 600 ng of the PCR product from control and Vcl CRISPR-KO cells was annealed separately by heating to 95 °C for 5 min, followed by cooling to 85 °C at a rate of 2 °C/sec and then it was further cooled to 25 °C at a rate of 0.1 °C/sec until the reaction reached 4 °C. The annealed PCR products were then digested using T7 Endonuclease I (Catalog # M0302S, NEB, USA) at 37 °C for 15 min and analysed on a 2% agarose gel.

Immunocytochemistry

Neurons were fixed using 4% PFA + 4% sucrose in PBS for 20 min and washed in PBS, 2 × 10 min. The cells were permeabilised with 0.1% Triton- × 100 in PBS for 5 min and blocked with 10% BSA in PBS for 30 min at room temperature with gentle rocking. Primary antibody incubation was done in 3% BSA for 1 h at 4 ºC with gentle rocking and then washed with PBS, 3 × 2 min. Secondary antibody incubation was done in 3% BSA for 30 min at room temperature, washed with PBS, 3 × 2 min and mounted with VECTASHIELD mounting medium with DAPI (#H-1000, Vector Laboratories, USA). The following primary antibodies were used: anti-GFP (#GFP-1020, 1:1000, Aves labs, Inc. USA), anti-β-III tubulin (#Tuj, 1:1000, Aves labs, Inc. USA), anti-Tau (#314,002, 1:1000, Synaptic Systems, Germany), anti-FAK (#5175, 1:250, Cell Signaling Technologies, USA) and anti-cofilin (#ab42824, 1:400, Abcam, USA). The following secondary antibodies from Invitrogen Inc. were used: Alexa Fluor (AF)-488 conjugated anti-chicken (# A11039, 1:1000), AF-594 conjugated anti-mouse (#A21203, 1:1000), AF-647 conjugated anti-rabbit (# A11012, 1:1000).

Phalloidin staining

Rhodamine-phalloidin (#6876, 1:125, Setareh Biotech, USA) was added along with secondary antibody during immunocytochemistry.

Immunohistochemistry

Immunohistochemistry was done as follows: embryonic or postnatal brains were fixed by transcardial perfusion using ice-cold PBS followed by 4%PFA, post-fixed in 4% PFA overnight and then cryopreserved in 30% sucrose until the brains were saturated with sucrose and sunk to the bottom of the tube, and frozen at − 80 ºC until use. The frozen brains were sectioned at 20 µm thickness, collected on Superfrost plus slides (Brain Research Laboratories, USA) and dried overnight before staining. Blocking/permeabilization was done in blocking solution (3% bovine serum albumin + 0.3% Triton-X100 + 1% goat serum in PBS) for 1 h at RT. Primary antibody incubation was done in the blocking solution overnight at 4 ºC with gentle rocking and washed with PBS for 5 × 5 min. Secondary antibody was incubated in the blocking solution for 1 h at RT, washed with PBS for 5 × 5 min, and slides were mounted with VECTASHIELD mounting medium with DAPI (Vector Laboratories, USA). The following primary antibodies were used: anti-GFP (GFP-1020, 1:1000, Aves labs, Inc. USA), anti-Cux1 (#sc-13024, 1:50, Santa Cruz Biotechnology, USA). The following secondary antibodies from Invitrogen Inc. were used: AlexaFluor-488 conjugated anti-chicken (#A11039, 1:1000), AlexaFluor-594 conjugated anti-rabbit (#A11012, 1:1000).

Neuronal culture and transfection

Neocortex from C57Bl/6 J pups (postnatal day 1–3) was dissected in Hibernate-A medium (#A1247501, Gibco, USA), digested with papain (#LS003124, Worthington, USA) for 30 min at 30 °C and dissociated with micropipette tips in Neurobasal-A medium (#10,888,022) supplemented with glutaMAX (#35,050,061, Gibco, USA), B27 (#17,504,044, Gibco, USA) and 33 U/ml penicillin/streptomycin. The tissue was gently triturated, cells were pelleted by centrifugation, and washed twice with Hibernate-A medium. Cells were then plated at a density of 125 cells/mm^2 on coverglass (#41,001,112, Glaswarenfabrik Karl Hecht, Germany) coated with poly-L-lysine (# P2636, Sigma, USA) and laminin (#354,232, BD, USA). Poly-L-lysine (50 µg/ml) coating was done for 2 h at 37 ºC, washed thrice with

Milli-Q water and dried at RT for 15 min followed by laminin (10 µg/ml) coating for 2 h at 37 ºC. Cultures were incubated at 37 °C with 5% CO2. After allowing for cells to attach to poly-L-lysine coverglass (20 min post-plating), the medium was gently replaced with fresh neuronal culturing medium. After 4 days in culture, neurons were fixed in 4% PFA + 4% sucrose in PBS for 20 min. Neuronal transfection was done just before plating using Nucleofection (Lonza, Switzerland) according to the manufacturer's instructions.

Drug treatment

For inhibiting the Arp2/3 protein complex in vitro, the pharmacological inhibitor CK-666 (Sigma Aldrich, SML0006) was used at a concentration of 25 nM. CK-666 or DMSO (control) was added at 24 h after plating the neurons, and neurons were allowed to grow for 3 more days.

In utero electroporation

In utero electroporation for different mutant constructs of *Vcl* were done on embryonic day 14.5 (E14.5) in C57bl/6 J embryos by injecting 1-2 µl of 1 µg/µl DNA in the lateral ventricle of one of the cerebral hemispheres. Electroporation was done using ECM 830 square wave electroporation system (BTX, USA) using 5 mm tweezer electrodes. The following parameters were used: voltage, 50 V; pulse length, 50 ms; number of pulses, 5; pulse interval, 100 ms. The brains were harvested at either embryonic day 17.5 (E17.5) or at postnatal day 5 (P5) for immunostaining.

Fluorescence recovery after photobleaching (FRAP)

FRAP was performed on an inverted motorised fluorescence microscope (IX83 Olympus, Japan) equipped with a 100X 1.49 NA PL-APO objective and maintained at 37 ºC with the aid of a whole microscope temperature-controlled chamber. Neuronal primary cultures were loaded in an open chamber (Ludin chamber, Life Imaging Services, Switzerland). The image acquisition was controlled by MetaMorph (Molecular Devices). Image acquisition was performed by illuminating with 488 or 561 nm laser, and fluorescence was collected with filters to observes Green and Red fluorescence proteins in total internal reflection microscopy mode at 50 Hz (Gataca Systems, France). Photobleaching was done by using a 561 nm laser line for 60 ms in a circular region of diameter 20 pixels close to the end of the axon. For baseline normalisation, 10 images were acquired before photobleaching. To observe the fluorescence recovery, 400 frames were acquired after the photobleaching sequence. For comparison between different experiments average of prebleached values were normalised to zero. Percentage calculation and normalisation were performed using Microsoft Excel software. The recovery of fluorescence was fit to the One-Phase association equation in GraphPad Prism. The quantification of recovery of fluorescence, mobile fraction and T-half graphs were generated from the curve fitting.

Single-particle tracking (SPT)

Single-particle tracking using photoactivation was performed on live neurons expressing mEOS3.2 as previously described [57]. These cells were loaded in an open chamber and photoactivated using a 405 nm laser (Omicron, Gataca Systems, France), and the images were acquired using a 561 nm laser (Cobolt, Gataca Systems, France). The power of lasers was adjusted to keep the number of the stochastically activated molecules constant and well separated during the acquisition. Continuous acquisition of 20,000 frames of images at 50 Hz (20 ms) were captured using a sensitive EMCCD camera (Evolve, Photometric). Image acquisition was controlled using MetaMorph software (Molecular Devices). Super resolved intensity images and single-particle trajectories were obtained using custom-built analysis for high-density single-particle tracking, which were described previously [57].

Data analyses and quantifications

Western blot quantification was done by using ImageJ. Axon length was measured using the 'traced line' tool in MetaMorph software (Molecular Devices). Numbers of primary and secondary neurites in cultured neurons were counted using Sholl analysis for different *vinculin* mutants. Cell body area was measured using the 'trace area' tool in MetaMorph software (Molecular Devices). The number of cells in different layers of the cortex was counted in ImageJ by using the 'cell counter' plugin. GFP fluorescence intensity was measured from the cell soma of neurons using the 'traced region' tool in MetaMorph software (Molecular Devices). For counting the FAK and Cofilin density, the intensity threshold was used to select the labelled cell soma and axonal growth cone. The active region of the cell soma and growth cone was used to filter the puncta. To detect the puncta of focal adhesion points labelled with FAK and Cofilin, intensity threshold of average intensity + SD of intensity in the active region was used. The number of puncta per unit area (number per μm^2) was plotted for both. All the graphs were generated using GraphPad Prism software.

Statistical analyses

One-way ANOVA followed by Tukey's *post-hoc* test or two-tailed Student's *t* test was used to determine statistical differences between groups using GraphPad Prism software. Error bars in figures are mean ± SEM unless otherwise

stated. For the statistical difference between frequency distribution of logarithmic values of diffusion coefficients, we used the Kolmogorov–Smirnov test. Diffusion coefficients were compared by unpaired *t* test. Wilcoxon matched-pair signed-rank test was used to conclude the difference between MSD curves. The area under the curve was calculated and compared using the Mann–Whitney test.

Image acquisition

Fluorescent images were acquired using Nikon Eclipse 80i upright fluorescent microscope (Nikon Instruments, USA) and confocal LSM880 microscope (Zeiss, Germany). FAK and Cofilin images were acquired using IX83 Olympus inverted motorised fluorescence microscope (Olympus, Japan) at 100 × in TIRF illumination mode. Images were acquired and pseudo coloured using MetaMorph software (Molecular Devices) for Nikon Eclipse 80i and IX83 Olympus microscope and Zen software for confocal LSM880 microscope. For imaging dynamics of growth cones, live imaging was performed on IX83 Olympus inverted motorised fluorescence microscope (Olympus, Japan) using 100× in TIRF illumination and 561 nm filter. The chamber was maintained at 37 ºC with the aid of a whole microscope temperature-controlled chamber. Neuronal primary cultures were loaded in an open chamber (Ludin chamber, Life Imaging Services, Switzerland). The images were obtained sequentially with a frame rate of 50 Hz for 5 min using Metamorph software (Molecular Devices).

Supplementary Information The online version contains supplementary material available at https://doi.org/10.1007/s00018-021-03879-7.

Acknowledgements We thank the microscopy facility and the Central Animal Facility in the division of biological sciences for confocal imaging and animal care, respectively.

Author contributions NR conceived of the project and designed the experiments. PM performed all the experiments and analysed the data; VB and DN performed the super-resolution microscopy experiments and analysed the data. NR wrote the manuscript, and all authors commented on previous versions of the manuscript. All authors read and approved the final manuscript.

Funding This work was supported by the Department of Biotechnology (DBT)-IISc Partnership Program (N.R. and D.N.), Department of Biotechnology Genomics Engineering Taskforce (N.R. and D.N.), STAR program grant (D.N.), Indian Institute of Science Eminence Program, and University Grants Commission, India (D.N.). P.M. was supported by a fellowship from Council for Scientific and Industrial Research. V.B. was supported by a fellowship from the University Grants Commission, India.

Data availability All materials are available on request.

Code availability Not applicable.

Declarations.

Conflict of interest The authors declare that they have no conflict of interest.

Ethics approval All the procedures in this study were performed according to the rules and guidelines declared in the Compendium of CPCSEA 2018 by the Committee for the Purpose of Control and Supervision of Experimental Animals (CPCSEA), Ministry of Fisheries, Animal Husbandry and Dairying, India. The research protocol was approved by the Institutional Animal Ethics Committee (IAEC) of the Indian Institute of Science (Project No. CAF/Ethics/516/2016), allowing the use of animals for in vitro and in vivo studies.

Consent to participate Not applicable.

References

1. Dent EW, Gupton SL, Gertler FB (2011) The growth cone cytoskeleton in axon outgrowth and guidance. Cold Spring Harb Perspect Biol 3(3):a001800
2. Lian G, Sheen VL (2015) Cytoskeletal proteins in cortical development and disease: actin associated proteins in periventricular heterotopia. Front Cell Neurosci 9:99
3. Luo L (2002) Actin cytoskeleton regulation in neuronal morphogenesis and structural plasticity. Annu Rev Cell Dev Biol 18:601–635
4. Ishikawa R, Kohama K (2007) Actin-binding proteins in nerve cell growth cones. J Pharmacol Sci 105:6–11
5. Dent EW et al (2007) Filopodia are required for cortical neurite initiation. Nat Cell Biol 9:1347–1359
6. Kwiatkowski AV et al (2007) Ena/VASP is required for neuritogenesis in the developing cortex. Neuron 56:441–455
7. Letourneau PC, Pech IV, Rogers SL, Palm SL, McCarthy JB, Furcht LT (1988) Growth cone migration across extracellular matrix components depends on integrin, but migration across glioma cells does not. J Neurosci Res 21:286–297
8. Mierke CT (2009) The role of vinculin in the regulation of the mechanical properties of cells. Cell Biochem Biophys 53:115–126
9. Romero S, Le Clainche C, Gautreau AM (2020) Actin polymerisation downstream of integrins: signaling pathways and mechanotransduction. Biochem J 477:1–21
10. Calderwood DA, Yan B, de Pereda JM, Alvarez BG, Fujioka Y, Liddington RC, Ginsberg MH (2002) The phosphotyrosine binding-like domain of talin activates integrins. J Biol Chem 277:21749–21758
11. Garcia-Alvarez B, de Pereda JM, Calderwood DA, Ulmer TS, Critchley D, Campbell ID, Ginsberg MH, Liddington RC (2003) Structural determinants of integrin recognition by talin. Mol Cell 11:49–58
12. Atherton P et al (2015) Vinculin controls talin engagement with the actomyosin machinery. Nat Commun 6:10038
13. Ziegler WH, Liddington RC, Critchley DR (2006) The structure and regulation of vinculin. Trends Cell Biol 16:453–460
14. Johnson RP, Craig SW (1994) An intramolecular association between the head and tail domains of vinculin modulates talin binding. J Biol Chem 269:12611–12619
15. Johnson RP, Craig SW (1995) F-actin binding site masked by the intramolecular association of vinculin head and tail domains. Nature 373:261–264
16. Bakolitsa C et al (2004) Structural basis for vinculin activation at sites of cell adhesion. Nature 430:583–586

17. Borgon RA, Vonrhein C, Bricogne G, Bois PR, Izard T (2004) Crystal structure of human vinculin. Structure 12:1189–1197
18. Letourneau PC, Shattuck TA (1989) Distribution and possible interactions of actin-associated proteins and cell adhesion molecules of nerve growth cones. Development 105:505–519
19. Burridge K, Mangeat P (1984) An interaction between vinculin and talin. Nature 308:744–746
20. Menkel AR, Kroemker M, Bubeck P, Ronsiek M, Nikolai G, Jockusch BM (1994) Characterisation of an F-actin-binding domain in the cytoskeletal protein vinculin. J Cell Biol 126:1231–1240
21. Xu W, Baribault H, Adamson ED (1998) Vinculin knockout results in heart and brain defects during embryonic development. Development 125:327–337
22. Xu W, Coll JL, Adamson ED (1998) Rescue of the mutant phenotype by reexpression of full-length vinculin in null F9 cells; effects on cell locomotion by domain deleted vinculin. J Cell Sci 111(Pt 11):1535–1544
23. Demali KA (2004) Vinculin–a dynamic regulator of cell adhesion. Trends Biochem Sci 29:565–567
24. Thievessen I et al (2013) Vinculin-actin interaction couples actin retrograde flow to focal adhesions, but is dispensable for focal adhesion growth. J Cell Biol 202:163–177
25. Coll JL, Ben-Ze'ev A, Ezzell RM, Rodriguez Fernandez JL, Baribault H, Oshima RG, Adamson ED (1995) Targeted disruption of vinculin genes in F9 and embryonic stem cells changes cell morphology, adhesion, and locomotion. Proc Natl Acad Sci U S A 92:9161–9165
26. Varnum-Finney B, Reichardt LF (1994) Vinculin-deficient PC12 cell lines extend unstable lamellipodia and filopodia and have a reduced rate of neurite outgrowth. J Cell Biol 127:1071–1084
27. Sydor AM, Su AL, Wang FS, Xu A, Jay DG (1996) Talin and vinculin play distinct roles in filopodial motility in the neuronal growth cone. J Cell Biol 134:1197–1207
28. Li CL, Sathyamurthy A, Oldenborg A, Tank D, Ramanan N (2014) SRF phosphorylation by glycogen synthase kinase-3 promotes axon growth in hippocampal neurons. J Neurosci 34:4027–4042
29. Nadarajah B, Parnavelas JG (2002) Modes of neuronal migration in the developing cerebral cortex. Nat Rev Neurosci 3:423–432
30. Humphries JD, Wang P, Streuli C, Geiger B, Humphries MJ, Ballestrem C (2007) Vinculin controls focal adhesion formation by direct interactions with talin and actin. J Cell Biol 179:1043–1057
31. Cohen DM, Chen H, Johnson RP, Choudhury B, Craig SW (2005) Two distinct head-tail interfaces cooperate to suppress activation of vinculin by talin. J Biol Chem 280:17109–17117
32. Cohen DM, Kutscher B, Chen H, Murphy DB, Craig SW (2006) A conformational switch in vinculin drives formation and dynamics of a talin-vinculin complex at focal adhesions. J Biol Chem 281:16006–16015
33. Chandrasekar I, Stradal TE, Holt MR, Entschladen F, Jockusch BM, Ziegler WH (2005) Vinculin acts as a sensor in lipid regulation of adhesion-site turnover. J Cell Sci 118:1461–1472
34. Ferrere A, Vitalis T, Gingras H, Gaspar P, Cases O (2006) Expression of Cux-1 and Cux-2 in the developing somatosensory cortex of normal and barrel-defective mice. Anat Rec A Discov Mol Cell Evol Biol 288:158–165
35. Atherton P, Stutchbury B, Jethwa D, Ballestrem C (2016) Mechanosensitive components of integrin adhesions: role of vinculin. Exp Cell Res 343:21–27
36. Roca-Cusachs P, del Rio A, Puklin-Faucher E, Gauthier NC, Biais N, Sheetz MP (2013) Integrin-dependent force transmission to the extracellular matrix by alpha-actinin triggers adhesion maturation. Proc Natl Acad Sci USA 110:E1361–E1370
37. Le S et al (2017) Mechanotransmission and Mechanosensing of Human alpha-Actinin 1. Cell Rep 21:2714–2723
38. Mierke CT, Kollmannsberger P, Zitterbart DP, Smith J, Fabry B, Goldmann WH (2008) Mechano-coupling and regulation of contractility by the vinculin tail domain. Biophys J 94:661–670
39. Craig AM, Banker G (1994) Neuronal polarity. Annu Rev Neurosci 17:267–310
40. Bays JL, DeMali KA (2017) Vinculin in cell-cell and cell-matrix adhesions. Cell Mol Life Sci 74:2999–3009
41. Stevens GR, Zhang C, Berg MM, Lambert MP, Barber K, Cantallops I, Routtenberg A, Klein WL (1996) CNS neuronal focal adhesion kinase forms clusters that co-localise with vinculin. J Neurosci Res 46:445–455
42. Le Clainche C, Dwivedi SP, Didry D, Carlier MF (2010) Vinculin is a dually regulated actin filament barbed end-capping and side-binding protein. J Biol Chem 285:23420–23432
43. Blanchoin L, Pollard TD, Mullins RD (2000) Interactions of ADF/cofilin, Arp2/3 complex, capping protein and profilin in remodeling of branched actin filament networks. Curr Biol 10:1273–1282
44. Mullins RD, Heuser JA, Pollard TD (1998) The interaction of Arp2/3 complex with actin: nucleation, high affinity pointed end capping, and formation of branching networks of filaments. Proc Natl Acad Sci USA 95:6181–6186
45. Sturner, T. et al. (2019). Transient localisation of the Arp2/3 complex initiates neuronal dendrite branching in vivo. Development 146(7)
46. Hetrick B, Han MS, Helgeson LA, Nolen BJ (2013) Small molecules CK-666 and CK-869 inhibit actin-related protein 2/3 complex by blocking an activating conformational change. Chem Biol 20:701–712
47. Huttelmaier S, Bubeck P, Rudiger M, Jockusch BM (1997) Characterisation of two F-actin-binding and oligomerisation sites in the cell-contact protein vinculin. Eur J Biochem 247:1136–1142
48. Thompson PM et al (2014) Identification of an actin binding surface on vinculin that mediates mechanical cell and focal adhesion properties. Structure 22:697–706
49. Riedl J et al (2008) Lifeact: a versatile marker to visualise F-actin. Nat Methods 5:605–607
50. Zhang M et al (2012) Rational design of true monomeric and bright photoactivatable fluorescent proteins. Nat Methods 9:727–729
51. Wozniak MA, Modzelewska K, Kwong L, Keely PJ (2004) Focal adhesion regulation of cell behavior. Biochim Biophys Acta 1692:103–119
52. De Pascalis C, Etienne-Manneville S (2017) Single and collective cell migration: the mechanics of adhesions. Mol Biol Cell 28:1833–1846
53. Carisey A, Ballestrem C (2011) Vinculin, an adapter protein in control of cell adhesion signalling. Eur J Cell Biol 90:157–163
54. Ezzell RM, Goldmann WH, Wang N, Parashurama N, Ingber DE (1997) Vinculin promotes cell spreading by mechanically coupling integrins to the cytoskeleton. Exp Cell Res 231:14–26
55. Carisey A et al (2013) Vinculin regulates the recruitment and release of core focal adhesion proteins in a force-dependent manner. Curr Biol 23:271–281
56. Ziegler WH, Gingras AR, Critchley DR, Emsley J (2008) Integrin connections to the cytoskeleton through talin and vinculin. Biochem Soc Trans 36:235–239
57. Nair D, Hosy E, Petersen JD, Constals A, Giannone G, Choquet D, Sibarita JB (2013) Super-resolution imaging reveals that AMPA receptors inside synapses are dynamically organised in nanodomains regulated by PSD95. J Neurosci 33:13204–13224